

SF3B1 hotspot mutations confer sensitivity to PARP inhibition by eliciting a defective replication stress response

Received: 9 March 2023

Accepted: 26 June 2023

Published online: 31 July 2023

 Check for updates

Philip Bland¹, Harry Saville¹, Patty T. Wai¹, Lucinda Curnow², Gareth Muirhead¹, Jadwiga Nieminuszczy², Nivedita Ravindran¹, Marie Beatrix John¹, Somaieh Hedayat¹, Holly E. Barker^{1,9}, James Wright², Lu Yu², Ioanna Mavrommati¹, Abigail Read¹, Barrie Peck^{1,10}, Mark Allen³, Patrycja Gazinska¹, Helen N. Pemberton^{1,4}, Aditi Gulati^{1,4}, Sarah Nash¹, Farzana Noor¹, Naomi Guppy¹, Ioannis Roxanis¹, Guy Pratt⁵, Ceri Oldreive⁶, Tatjana Stankovic⁶, Samantha Barlow⁷, Helen Kalirai⁷, Sarah E. Coupland⁷, Ronan Broderick², Samar Alsafadi⁸, Alexandre Houy⁸, Marc-Henri Stern⁸, Stephen Pettit^{1,4}, Jyoti S. Choudhary², Syed Haider¹, Wojciech Niedzwiedz², Christopher J. Lord^{1,4} & Rachael Natrajan¹✉

SF3B1 hotspot mutations are associated with a poor prognosis in several tumor types and lead to global disruption of canonical splicing. Through synthetic lethal drug screens, we identify that *SF3B1* mutant (*SF3B1*^{MUT}) cells are selectively sensitive to poly (ADP-ribose) polymerase inhibitors (PARPi), independent of hotspot mutation and tumor site. *SF3B1*^{MUT} cells display a defective response to PARPi-induced replication stress that occurs via downregulation of the cyclin-dependent kinase 2 interacting protein (CINP), leading to increased replication fork origin firing and loss of phosphorylated CHK1 (pCHK1; S317) induction. This results in subsequent failure to resolve DNA replication intermediates and G₂/M cell cycle arrest. These defects are rescued through CINP overexpression, or further targeted by a combination of ataxia-telangiectasia mutated and PARP inhibition. In vivo, PARPi produce profound antitumor effects in multiple *SF3B1*^{MUT} cancer models and eliminate distant metastases. These data provide the rationale for testing the clinical efficacy of PARPi in a biomarker-driven, homologous recombination proficient, patient population.

Somatic mutations in components of the RNA splicing machinery occur across a variety of hematologic malignancies and solid tumors, highlighting the significance of aberrant splicing to tumorigenesis^{1,2}. Heterozygous somatic hotspot mutations in the spliceosomal component *SF3B1* are the most common of these and occur at high frequencies in patients with myelodysplastic syndromes (20%), chronic lymphocytic leukemia (CLL; 15%), acute myeloid leukemia (AML; 3%) and in solid tumors such as uveal melanoma (20%), cutaneous melanoma (4%)

and breast (2%), pancreatic (2%), lung (2%) and prostate cancer (1%)^{3–13}. Hotspot *SF3B1* mutations are associated with poor patient outcomes in CLL, AML, uveal melanoma and breast cancer^{14–18}. The *SF3B1* gene encodes subunit 1 of splicing factor 3b, a component of the U2 small nuclear ribonucleoprotein, which is involved in catalyzing precursor mRNA to mature transcripts. *SF3B1* contains several HEAT domains (Huntingtin, Elongation factor 3, protein phosphatase 2A and Target of rapamycin 1), which are hotspots for most somatic mutations^{1,2,8,19–22}.

A full list of affiliations appears at the end of the paper. ✉ e-mail: rachael.natrajan@icr.ac.uk

Hotspot mutations in *SF3B1* are neomorphic, inducing conformation changes in the HEAT superhelix domain that alters the interaction of SF3B1 with the pre-mRNA sequence²³. As such, mutations result in reduced branchpoint fidelity, leading to the use of cryptic 3' splice sites that lead to global aberrant splicing. Many of these transcripts are degraded via nonsense-mediated decay leading to the downregulation of mRNA and canonical proteins, while others produce aberrant proteins^{1,8,19–22}. A large proportion of the alternative splicing events are conserved among multiple tumor types regardless of the mutated amino acid^{21,24}, and although these events have been comprehensively cataloged, their functional impact is largely uncharacterized.

SF3B1 mutant (*SF3B1*^{MUT}) cells have been reported to rely on the wild-type allele for survival, while the heterozygous hotspot mutation leads to a neomorphic function, which does not produce a conventional oncogene addiction²⁵. This suggests that therapeutic inhibition of the spliceosome may have a clinical benefit, particularly given many *SF3B1*^{MUT} cancers have few effective treatments²⁵. We and others have demonstrated that *SF3B1*^{MUT} cancers are selectively sensitive to SF3b complex inhibitors both in vitro and in vivo^{1,8,26,27}, which has led to clinical efforts to directly inhibit the spliceosome in patients with refractory leukemia. However, preliminary clinical studies have shown minimal patient responses^{28,29}, suggesting other therapeutic approaches are warranted. Recent studies have identified aberrant splicing events that alter the maturation of the constitutive transcript and subsequent protein production of several genes. These lead to a failure in producing full-length proteins of a number of oncogenes and tumor suppressor genes, and consequently render *SF3B1*^{MUT} cells vulnerable to therapeutic intervention^{30–33}. However, the clinical implementation of some of these approaches may be challenging.

Results

SF3B1^{MUT} cells show selective sensitivity to PARP inhibitors

To identify candidate therapeutic targets for cancers with *SF3B1* hotspot mutations, we utilized the leukemia K562^{K700E} (*SF3B1*^{K700E}) and parental (*SF3B1*^{WT}) isogenic cells¹, to model one of the most prevalent *SF3B1* hotspot mutations seen in patients^{8,19,20} (Fig. 1a,b and Supplementary Fig. 1a). Using a drug-sensitivity screen, with an in-house curated library of 80 small-molecule inhibitors, we identified a series of candidate *SF3B1*^{MUT} synthetic lethal drugs, where at least two different concentrations significantly led to reduced survival in *SF3B1*^{K700E} cells³⁴ (survival fraction ratio K562^{K700E}/K562^{WT} cells < 0.6 and $P < 0.01$, unpaired two-tailed t -test; Fig. 1c and Supplementary Table 1). These included talazoparib (PARPi), gemcitabine, vinorelbine and SAR-20106 (CHK1 inhibitor; Fig. 1d and Supplementary Table 1). Subsequent validation in multiple isogenic cells with different hotspot mutations¹⁹ identified a robust association with multiple PARPi, whereas additional hits from the screen failed to validate (Fig. 1e,f, Extended Data Fig. 1a–d and Supplementary Fig. 1b,c). PARPi sensitivity was also observed in the endogenously mutated uveal melanoma cell

line MEL202 harboring the most common uveal melanoma *SF3B1*^{R625G} hotspot variant¹⁹ compared to a series of *SF3B1*^{WT} uveal melanoma cells (Fig. 1g and Extended Data Fig. 1e,g).

To confirm on-target effects, we used MEL202 *SF3B1*^{R625G} cells to knock in an inducible degron tag sequence (Degron-KI) into the single *SF3B1*^{MUT} allele as previously described²⁵. In normal growth conditions, the mutant SF3B1 protein undergoes proteasomal degradation, and cells solely express the wild-type SF3B1 protein²⁵ (MEL202^{R625G}DD-SF3B1, hereafter termed MEL202^{R625G}-DEG (mutant degraded)). Exposure to the small-molecule ligand Shield-1 stabilized the degron-tagged mutant protein and reversed the aberrant splicing of the indicator transcript *CRNDE*. The continuous degradation of the *SF3B1*^{MUT} protein in these cells led to the loss of PARPi sensitivity, highlighting that mutant *SF3B1* influences PARPi response (Fig. 1g and Extended Data Fig. 1f).

We next used a genome-wide PARPi resistance (100 nM talazoparib) CRISPR knockout screen to gain mechanistic insights into the observed PARPi sensitivity in K562^{K700E} cells (Fig. 1h,i, Extended Data Fig. 1i,j and Supplementary Table 2). In agreement with previous studies^{35,36}, *PARP1* knockout led to PARPi resistance but had no significant effect on untreated cell viability (Fig. 1h,i, Extended Data Fig. 1k,l and Supplementary Table 2). Exposure to the PARP1 catalytic inhibitor veliparib showed limited sensitivity, compared to the more potent PARP-trapping agents, in *SF3B1*^{MUT} cells (Extended Data Figs. 1m and 2a,b). None of the previously identified genes, which were found to mediate PARPi resistance in homologous recombination-deficient *BRCA1*-defective cells³⁷, was significant in the knockout screen (Fig. 1h and Extended Data Fig. 2c). Consistent with this, *SF3B1*^{MUT} cells maintained their ability to form nuclear RAD51 foci at the sites of DNA damage, in contrast to the homologous recombination-deficient SUM149 *BRCA1*^{MUT} cells (Extended Data Fig. 2d), confirming that PARPi sensitivity in *SF3B1*^{MUT} cells is not driven by a possible deficiency in the homologous recombination machinery. Of note, there was no difference in SF3B1 protein expression between *SF3B1*^{WT} and *SF3B1*^{MUT} cells \pm cycloheximide, suggesting that *SF3B1* hotspot mutations do not impact the protein expression or stability of SF3B1 (Extended Data Fig. 2e). Additionally, exposure of MEL202^{R625G}-DEG cells to the potent SF3B1 inhibitor Pladienolide B in combination with talazoparib did not sensitize MEL202^{R625G}-DEG cells to the same degree as single-agent PARPi exposure in MEL202^{R625G} cells. This agrees with existing data that *SF3B1* mutations are neomorphic rather than loss of function^{1,25} (Extended Data Fig. 1f).

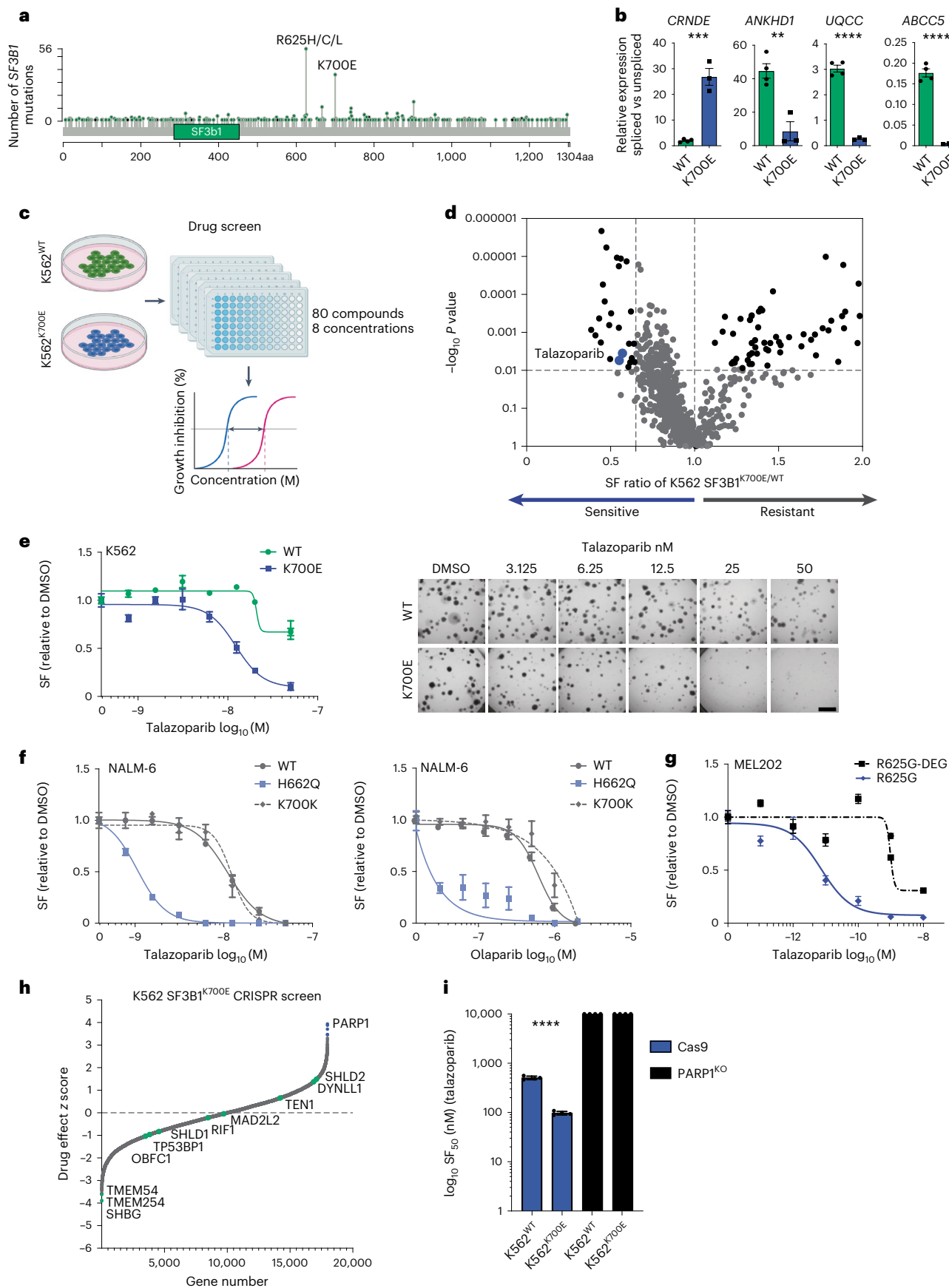
SF3B1^{MUT} cells show dysregulation of ATR pathways

We sought to ascertain whether *SF3B1*^{MUT} cells showed changes in their repertoire of aberrant splicing events when exposed to PARPi. As previously described, K562^{K700E} cells had distinct transcriptomes, typified by unique changes to RNA splicing^{1,8,18,19,21} (Extended Data Fig. 3a). PARPi exposure, however, resulted in only 17 significant differential splicing

Fig. 1 | *SF3B1* hotspot mutations lead to PARPi sensitivity in isogenic models.

a, Lollipop plot of the number of *SF3B1* mutations in TCGA (pan-cancer cohort and MSP IMPACT clinical sequencing study ($n = 21,912$)). Data from cBioportal. **b**, qRT-PCR of differentially spliced exons of selected indicator genes in the myeloid leukemia isogenic cell lines (K562) that express wild-type (WT) or mutant (K700E) *SF3B1* ($n = 3$ independent biological replicates). Data are mean \pm s.e.m., unpaired two-tailed t -test; *CRNDE*, $P = 0.0003$; *ANKHDI*, $P = 0.0036$; *UQCC*, $P < 0.0001$ and *ABCC5*, $P < 0.0001$. **c**, Schematic of small-molecule inhibitor screening pipeline. **d**, Volcano plot of compound selectivity from the small-molecule inhibitor library screen in K562 cell lines ($-\log_{10} P < 0.01$ unpaired two-tailed t -test and surviving fraction (SF) ratio K562 *SF3B1*^{K700E}/*SF3B1*^{WT} < 0.6). Blue dots indicate two independent concentrations of the PARPi talazoparib. **e**, Fourteen-day clonogenic dose–response curves and representative images of K562 isogenic cells harboring the K700E *SF3B1* hotspot variant and wild-type cells following exposure with the PARPi talazoparib (scale bar = 4 mm). **f**, Fourteen-day clonogenic dose–response curves of NALM-6

isogenic cells with the H662Q *SF3B1* hotspot variant, K700K silent variant and wild-type cells following exposure with talazoparib and olaparib ($n = 3$ independent biological replicates, error bars show \pm s.e.m.). **g**, Fourteen-day clonogenic dose–response curves of uveal melanoma MEL202^{R625G} cells with the endogenous R625G *SF3B1* hotspot variant, and revertant MEL202^{R625G}-DEG cells following exposure with talazoparib. Data are mean normalized to DMSO control from $n = 3$ independent biological experiments, error bars show \pm s.e.m. (**e–g**). **h**, Waterfall plot of whole-genome CRISPR screen in K562 *SF3B1*^{K700E} cells, depicting hits (blue) from $n = 3$ independent biological replicate experiments. Genes known to cause resistance to PARPi in homologous recombination-deficient cells are highlighted. **i**, Bar plot depicting the SF₅₀ (concentration of drug that allows 50% cell survival) values of K562 *SF3B1* wild-type and K700E cells with Cas (control) or CRISPR *PARP1*^{KO} under talazoparib exposure ($n = 3$ independent biological repeats). Error bars show mean \pm s.e.m. Unpaired two-tailed t -test, Cas9 wild-type versus K700E. * $P < 0.05$, ** $P < 0.01$, *** $P < 0.001$, **** $P < 0.0001$ (**b,i**). SF, surviving fraction.



events and no changes in alternative splice site 3' splice site recognition upon PARPi exposure (Extended Data Fig. 3a,b and Supplementary Tables 3 and 4), suggesting that PARPi exposure does not alter global splicing decisions in *SF3B1*^{MUT} cells. Differential gene expression analysis similarly highlighted that PARPi induces minor transcriptional changes (Fig. 2a). Gene set enrichment analysis (GSEA) of the small number of differentially expressed genes identified that K562^{K700E} cells showed specific dysregulation of genesets involved in transcription, DNA replication and the cell cycle compared to K562^{WT} cells only when exposed to PARPi (Supplementary Fig. 2a,b and Supplementary Tables 3 and 4), suggesting that *SF3B1*^{MUT} cells stop cycling and consequently alter their DNA replication and transcription upon PARPi exposure. Moreover, assessment of genome-wide RNA Pol II binding through ChIP-sequencing highlighted that *SF3B1*^{MUT} cells do not have an innate transcriptional activity defect (that is no observed differential global RNA Pol II binding in untreated *SF3B1*^{WT} versus *SF3B1*^{MUT} cells), which could contribute to PARPi sensitivity in these cells (Extended Data Fig. 3c–e and Supplementary Table 5).

We then assessed what effects PARPi exposure had on the proteome of the MEL202^{R625G} and isogenic MEL202^{R625G-DEG} cells. As MEL202^{R625G} cells possess a naturally occurring *SF3B1* hotspot mutation; they have been shown to display the conserved mis-splicing signature associated with *SF3B1*^{K700E} hotspot variations^{1,19}; and were the most sensitive to PARPi, we reasoned that any differences in these cells would be marked further upon PARPi exposure (Supplementary Fig. 2c,d). Quantitative high-content peptide mass spectrometry ±PARPi identified that 54% of the proteome (4788/8856 identified proteins) was differentially expressed in MEL202^{R625G} compared to MEL202^{R625G-DEG} cells (Supplementary Table 6). GSEA analysis failed to identify any differentially enriched pathways between MEL202^{R625G} and MEL202^{R625G-DEG} cells exposed to DMSO; however, G₂/M checkpoint, apoptosis and E2F target genesets were selectively enriched after 48 h of 50 nM PARPi exposure in MEL202^{R625G} cells (Fig. 2b,c and Extended Data Fig. 4a). The mass spectrometry data additionally identified several ataxia-telangiectasia mutated and Rad3-related (ATR) pathway-related proteins as significantly downregulated in MEL202^{R625G} compared to MEL202^{R625G-DEG} cells (log₂-transformed fold change < -2), including DYRK2, RAD9A, CINP, TTI1, TTI2 and NEK1. Of these, CINP was further downregulated upon PARPi exposure and was the most downregulated protein in MEL202^{R625G} cells compared with MEL202^{R625G-DEG} cells exposed to PARPi (Fig. 2b and Supplementary Table 6). CINP is associated with genome maintenance and found to transiently interact with ATRIP-ATR, although not specifically, under UV-induced DNA damage³⁸. CINP protein expression was downregulated in multiple *SF3B1*^{MUT} cells and patient-derived uveal melanoma models compared to *SF3B1*^{WT} models (Fig. 2d–f, Extended Data Fig. 4b and Supplementary Fig. 2e). This association was also validated in primary *SF3B1*^{K700E} patients, who were treated with single-agent olaparib as part of the dose-finding phase I PiCCLe clinical trial³⁹. Three of the four *SF3B1*^{MUT} patients had the longest progression-free survival time on olaparib and showed loss of CINP protein expression (Fig. 2g,h).

Analysis of mis-spliced events that were identified in *SF3B1*^{MUT} primary cancers harboring multiple hotspot mutations from published studies^{2,15}, that were also identified in the MEL202^{R625G} cells, failed to identify any mRNA downregulation or aberrant splicing event of CINP, which may explain the observed reduction in protein levels (Supplementary Fig. 2f and Supplementary Table 4). We also did not identify any significant alternative splicing event of additional genes directly involved in the ATR pathway (Supplementary Table 7). Moreover, MEL202^{R625G-DEG} and MEL202^{R625G} cells expressed similar levels of ATRIP (immediate interactor of CINP), following short-term DMSO or PARPi exposure (Extended Data Fig. 4c). Additionally, we observed no stabilization of CINP protein expression in MEL202^{R625G} cells upon inhibition of nonsense-mediated decay (cycloheximide) or proteasome inhibition (MG-132; Extended Data Fig. 4d).

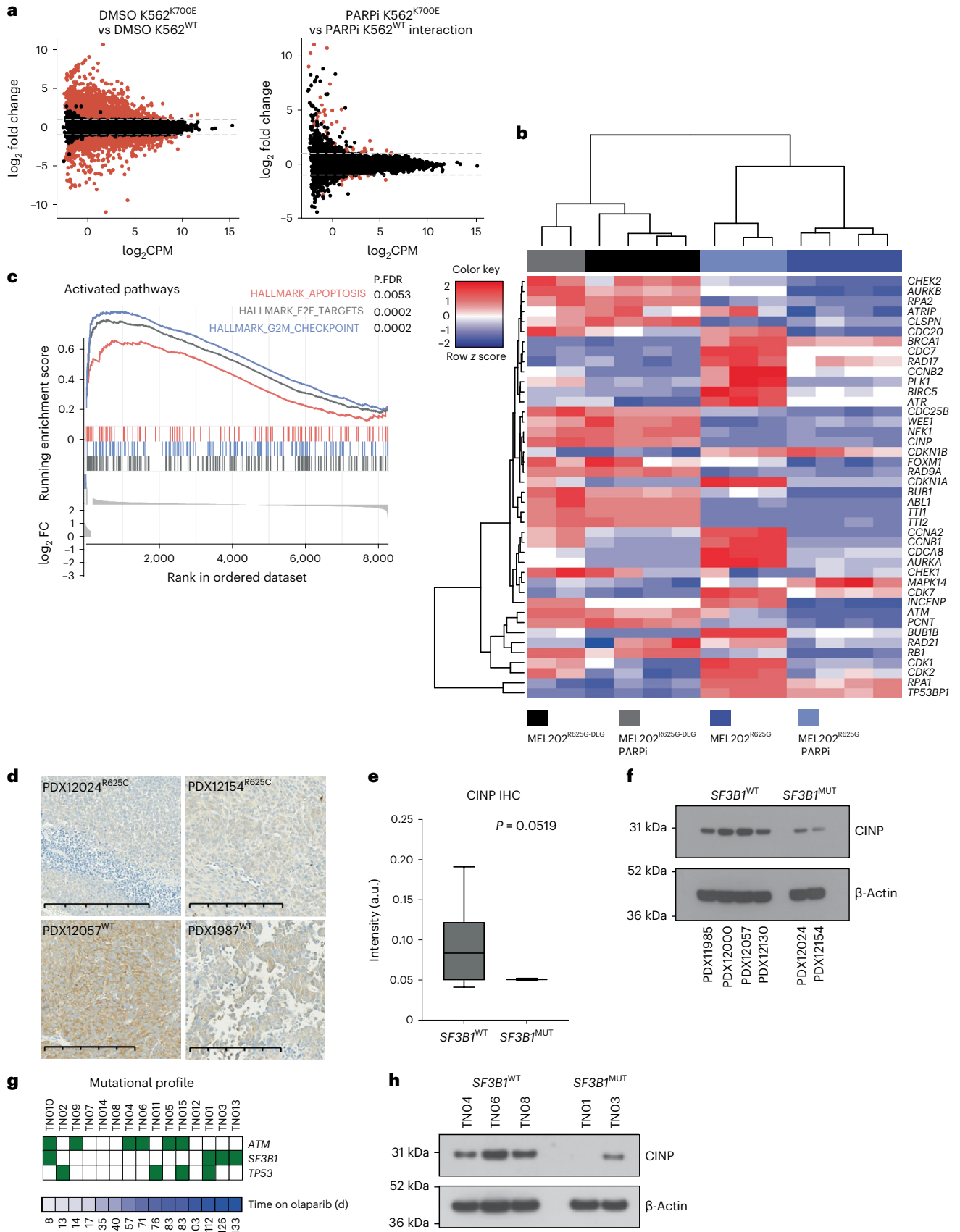
SF3B1^{MUT} cells show a defective replication stress response

Given the observed G₂/M checkpoint induction in MEL202^{R625G} cells and the downregulation of proteins involved in the ATR-mediated replication stress response, we evaluated whether *SF3B1*^{MUT} cells have defects in replication stress^{40,41}. Using DNA-fiber assays to assess DNA replication origin firing, fork speed and symmetry^{42,43}, we observed no difference in the number of origins, fork speed or sister fork ratio under normal growth conditions. However, (3 h) PARPi exposure in MEL202^{R625G} cells resulted in a sustained number of newly firing replication origins (as verified upon CDC7 inhibition), a significant increase in fork speed and an increase in the sister fork ratio (that is, fork asymmetry) compared to MEL202^{R625G-DEG} cells (Fig. 3a–d and Extended Data Fig. 5a,b). As such, (1–3 h) PARPi exposure resulted in reduced induction of pCHK1 (S317) and pATR (T1989) in MEL202^{R625G} and K700E^{K700E} cells, whereas MEL202^{R625G-DEG}, MP41^{WT} and K562^{WT} cells showed a time-dependent induction of the replication stress response. This was coupled with a decrease in pRPA2 (S33) and an increase in total RPA foci in *SF3B1*^{MUT} cells, highlighting an increase in DNA/RPA complexes due to perturbed replication (replication stress following PARPi exposure; Fig. 3e,f and Extended Data Fig. 5c,d).

CINP gene silencing similarly resulted in an impaired pCHK1 (S317) response and caused sensitivity to PARPi in MEL202^{R625G-DEG} cells (Fig. 4a,b and Extended Data Fig. 5e). Of note, *CINP* gene silencing did not significantly further the sensitivity of MEL202^{R625G} cells to talazoparib. Hydroxyurea, known to collapse replication forks, did not reproduce this defective response, as fork symmetry (CldU/IdU) and pCHK1 (S317) induction were comparable between MEL202^{R625G-DEG} and MEL202^{R625G} cells. Furthermore, cell survival after hydroxyurea or gemcitabine addition showed no selectivity for MEL202^{R625G} cells, indicating that PARPi sensitivity in *SF3B1*^{MUT} cells is driven by a defective replication stress response to an increase in fork origin firing and subsequent accelerated replication, rather than innate replication stress (Extended Data Figs. 5f and 6a–c). Reconstitution of CINP protein expression in MEL202^{R625G} cells (MEL202^{R625G}-CINP-GFP) resulted in restoration of the canonical replication stress response to PARPi (pCHK1 (S317) induction and reversal of PARPi sensitivity),

Fig. 2 | *SF3B1*^{MUT} cells show transcriptional dysregulation and the induction of G₂/M checkpoint proteins when exposed to PARPi. a, MA plots highlighting the significantly differentially expressed genes between the highlighted comparisons in the K562 RNA-sequencing data (DMSO K562^{K700E} versus DMSO K562^{WT} changes just due to the *SF3B1* mutation and PARPi K562^{K700E} versus PARPi K562^{WT} interaction; changes due to the effect of PARPi only accounting for the genotype-specific effects). Significantly differentially expressed genes are depicted in red (FDR < 0.01, |LFC| > 1). **b**, Heatmap representing mean-centered, hierarchical clustering of proteins and samples mapping to the ATR pathway from the total-MS/MS. **c**, Gene set enrichment plot from GSEA analysis of total-MS/MS of MEL202^{R625G} and MEL202^{R625G-DEG} isogenic cell lines after DMSO or 50 nM talazoparib exposure for 48 h. *P* values shown are FDR corrected.

d, Representative micrographs of CINP IHC in *SF3B1*^{MUT} and *SF3B1*^{WT} PDX models. Scale bar, 200 μm. **e**, Box and whiskers plot of the digital quantification of CINP IHC across *SF3B1*^{MUT} (*n* = 3) and *SF3B1*^{WT} (*n* = 8) PDX models (*P* = 0.0519, Welch's unpaired two-tailed *t*-test). **f**, Western blot of CINP from *SF3B1*^{MUT} and *SF3B1*^{WT} PDX lysates and β-actin loading control. **g**, Heatmap depicting the distribution of genetic alterations in CLL driver genes: *ATM*, *SF3B1* and *TP53* aligned according to time on olaparib treatment. Presence of mutations is highlighted by green shaded boxes. Modified from ref. 39. **h**, Western blot of CINP expression in *SF3B1*^{WT} and *SF3B1*^{K700E} patients enrolled in the PiCCLe trial collected at baseline and exposed to PARPi for 48 h in vitro before lysis and western blot analysis. *P* values shown are calculated with chi-square test (**d**). IHC, immunohistochemistry.



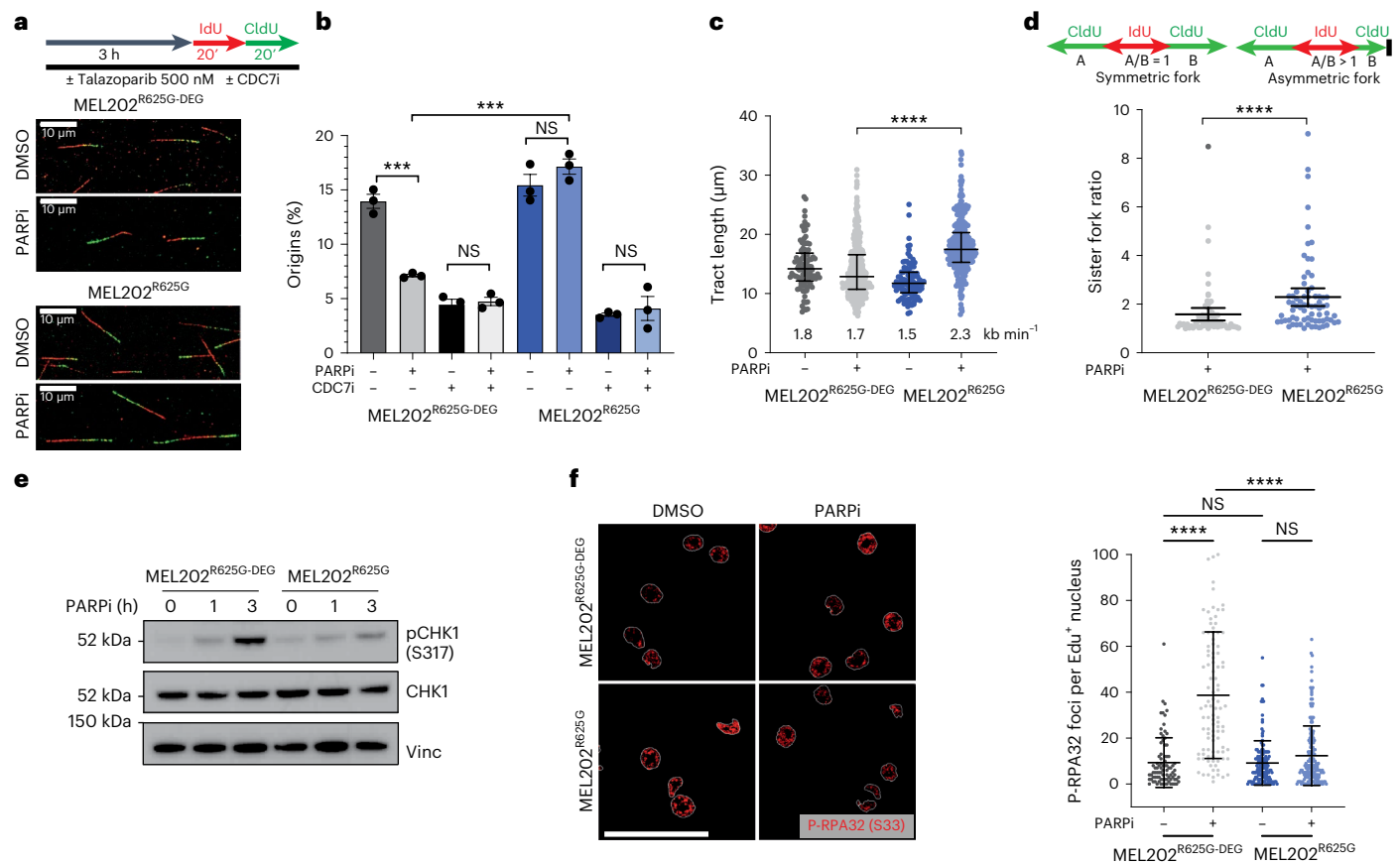


Fig. 3 | *SF3B1*^{MUT} cells elicit a defective replication stress response following PARPi exposure. **a**, Experimental setup of fiber assay. Cells were pre-incubated with 500 nM talazoparib for 3 h, followed by sequential labeling with 25 μ M IdU (red) and 125 μ M CldU (green). Representative immunofluorescence images of individual fibers highlighting the differences in tract length. **b**, Bar plot showing percentage of newly firing origins from IdU and CldU labeled DNA fibers after 3 h 500 nM talazoparib or DMSO or combination 500 nM talazoparib and 20 μ M CDC7i XL413. A minimum of 400 replication structures were scored across $n = 3$ biologically independent experiments and the percentage of origins was calculated in each of the replicate experiments. *** $P = 0.0005$ and *** $P = 0.0002$ (left to right), unpaired two-tailed t -test. **c**, Scatterplot of fork speed (tract length). **d**, Schematic of scoring and scatterplot of sister fork ratio. Fork

symmetry was analyzed by calculating the ratio of the leftward and rightward tracts emanating by sister forks emerging from the same replication origin; A/B ratio >1 indicates for fork asymmetry and increased fork stalling. Data are mean of $n = 3$ biological replicates, error bars show \pm s.e.m. P value determined by unpaired two-tailed t -test. **e**, Western blot of CHK1 phosphorylation at serine 317 (pCHK1 (S317)), and total CHK1 expression in MEL202 isogenic cells, after 0, 1 and 3 h of 500 nM talazoparib exposure. Images are representative of $n = 3$ biological replicates. **f**, Representative immunofluorescence images (left) and scatterplot (right) of pRPA32 (S33) foci in MEL202 isogenic cells following 3 h of 500 nM talazoparib or DMSO exposure. Data are from $n = 2$ biological replicates, error bars show \pm s.d. of foci in individual nuclei. Scale bar, 50 μ m. P values determined by unpaired two-tailed t -test. *** $P < 0.001$, **** $P < 0.0001$. NS, not significant.

validating that the defective replication stress response is directly due to low levels of CINP in *SF3B1*^{MUT} cells (Fig. 4c,d and Supplementary Fig. 4a).

We next investigated the consequence of the *SF3B1*^{MUT}-specific replication stress response. MEL202^{R625G-DEG} and K562^{WT} cells displayed robust recruitment of 53BP1 and γ H2AX foci after 3 h PARPi exposure, coinciding with pCHK1 (S317) activation. MEL202^{R625G} and K562^{K700E} cells failed to recruit 53BP1 upon 3 h PARPi exposure, paralleling their lack of pCHK1 (S317) induction, although showed γ H2AX induction, indicative of the duality of 53BP1. However, after 48 h PARPi exposure, the majority of MEL202^{R625G} and K562^{K700E} cells induced 53BP1 and showed sustained γ H2AX foci, whereas *SF3B1*^{WT} cells resolved these foci (Fig. 4e,f and Extended Data Fig. 7a,b). These phenotypes were reversed upon CINP overexpression (Extended Data Fig. 7c,d) and in accordance with the pCHK1 (S317) response were not recapitulated under hydroxyurea exposure (Extended Data Fig. 7e,f).

We then sought to address whether the defective replication stress response observed in *SF3B1*^{MUT} cells persists due to incomplete fork repair and replication. Using FANCD2 foci formation as a marker of

unresolved replication intermediates, we observed no significant increase in FANCD2 foci in MEL202^{R625G-DEG} cells exposed to PARPi compared to DMSO controls. This was coupled with an increase in the percentage of MUS81-positive FANCD2 foci, indicative of the resolution of replication intermediates^{44,45} (Fig. 4g,h and Extended Data Fig. 8a). MEL202^{R625G} cells, however, showed a significant increase in the number of FANCD2 foci after PARPi exposure and a reduction of MUS81-positive FANCD2 foci. This is suggestive of impaired recruitment to damaged forks, which results in incomplete replication and unresolved replication intermediates in *SF3B1*^{MUT} cells. Accordingly, siRNA-mediated silencing of *MUS81* in MEL202^{R625G} cells induced no further sensitivity to PARPi, in contrast to the observed interaction of *MUS81* silencing in *BRCA* mutant cells⁴⁶ (Extended Data Fig. 8b,c). These markers of unresolved fork structures were observed under the same PARPi concentration and exposure time as the total mass spectrometry dataset, indicating that after failing to activate a canonical replication stress response to PARPi, *SF3B1*^{MUT} cells express proteins integral to the G₂/M checkpoint.

Rescue of the defective replication stress response was additionally validated through the generation of an independent

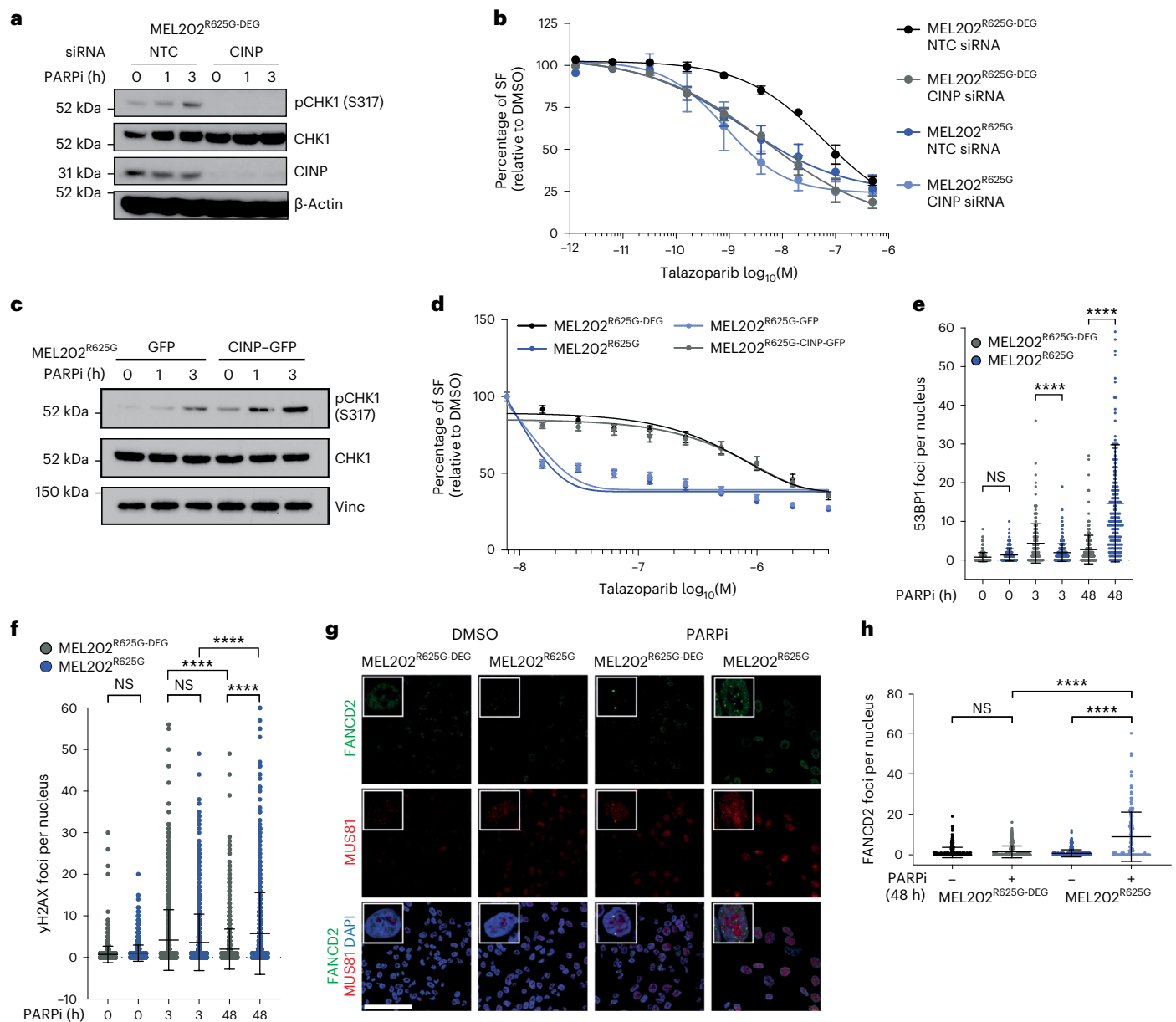


Fig. 4 | A defective replication stress response leads to PARPi sensitivity in *SF3B1*^{MUT} cells. **a, Western blot of pCHK1 (S317), total CHK1 and CINP expression in MEL202^{R625G-DEG} cells after non-targeting control (NTC) or *CINP* siRNA-mediated gene silencing, with 0, 1 or 3 h of 500 nM talazoparib exposure. Images are representative of $n = 3$ biological replicates. **b**, Talazoparib dose-response curves showing the SF, relative to DMSO, of MEL202 isogenic cells after NTC or *CINP* siRNA-mediated gene silencing. Data are mean of three replicates, error bars show \pm s.e.m. **c**, Western blot of pCHK1 (S317) and total CHK1 expression in MEL202^{R625G} cells expressing control-GFP or CINP-GFP, following 0, 1 and 3 h of 500 nM talazoparib exposure. Images are representative of two biological replicates. **d**, Talazoparib dose-response curves showing the SF, relative to**

DMSO, of MEL202 isogenic cells, and MEL202^{R625G} cells expressing control-GFP or CINP-GFP. Data are mean of $n = 3$ biological replicates, error bars show \pm s.e.m. **e, f**, Scatterplots showing the number of 53BP1 (**e**) and γ H2AX (**f**) foci per nucleus in MEL202 isogenic cells after 0, 3 h (500 nM) and 48 h (50 nM) talazoparib exposure. Data are representative of $n = 3$ biological replicates, error bars show \pm s.d. **g, h**, Representative immunofluorescence images (**g**) of FANCD2 and MUS81 foci and scatterplot of FANCD2 foci (**h**) in MEL202 isogenic cells after 48 h DMSO or (50 nM) talazoparib exposure. Scale bar, 100 μ m. Data are representative of $n = 3$ biological replicates, error bars show \pm s.d. of individual nuclei assessed. *P* values are calculated by one-way ANOVA (**e, f** and **h**), *****P* < 0.0001. NTC, nontargeting control; NS, not significant.

CINP overexpressing cell line model (Extended Data Fig. 8d–i). MEL202^{R625G} and K562^{K700E} cells were not selectively sensitive to single-agent ATR or CHK1 inhibition, suggesting that replication-induced R loops resulting in ATR activation are not a primary mechanism of sensitivity in *SF3B1*^{MUT} cells^{47,48} (Supplementary Figs. 1c and 4b). Together, these results indicate that PARPi sensitivity in *SF3B1*^{MUT} cells is driven by a defective replication stress response to increased fork origin firing and incomplete resolution of replication intermediates.

SF3B1^{MUT} cells stall in G₂/M upon PARPi exposure

Finding that *SF3B1*^{MUT} cells harbor markers of unresolved replication intermediates upon PARPi exposure, and that temporally this coincides with the induction of G₂/M checkpoint proteins in the mass spectrometry analysis, we performed a cell cycle analysis \pm PARPi. Propidium iodide staining and fluorescence-activated cell sorting (FACS) analysis showed a similar cell cycle profile in MEL202^{R625G-DEG} and MEL202^{R625G} cells. Upon 48 h PARPi exposure, MEL202^{R625G} cells showed a significant increase in the percentage of cells in G₂/M, which

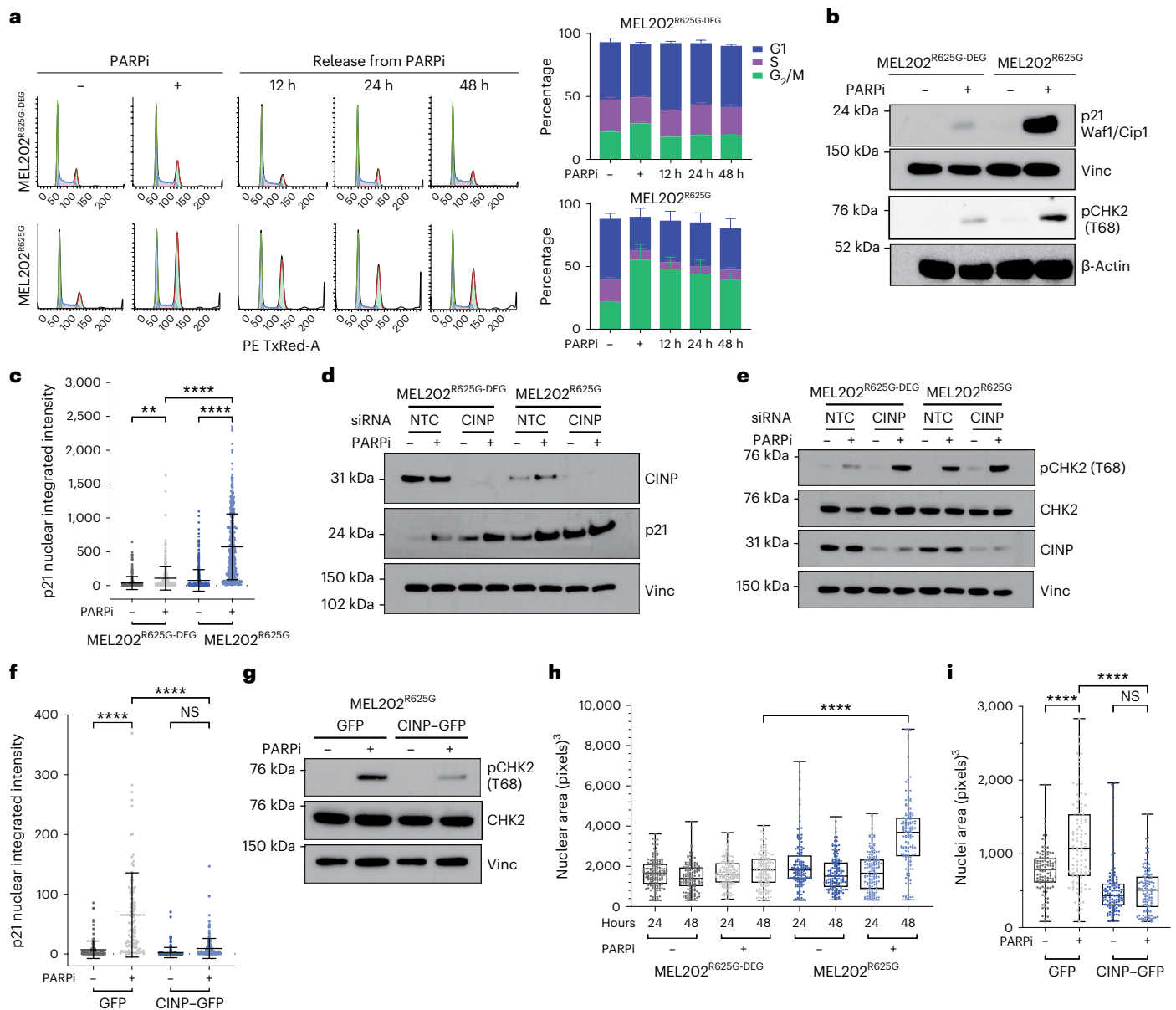


Fig. 5 | PARP inhibition leads to G₂/M checkpoint stalling in *SF3B1*^{MUT} cells.

a, Flow cytometry histograms of propidium iodide staining and stacked bar plots, showing the cell cycle profile of MEL202 isogenic cells after 48 h of 50 nM talazoparib exposure, and 12, 24 and 48 h after subsequent talazoparib removal. Data are mean of $n = 3$ biological replicates, error bars show \pm s.e.m. **b**, Western blot of p21^{Waf1/Cip1} and CHK2 phosphorylation (threonine68 (pCHK2 (T68))) in MEL202 isogenic cells after 48 h of 50 nM talazoparib or DMSO exposure. Images are representative of $n = 3$ biological replicates. **c**, Scatterplot quantification of nuclear intensity of p21 in MEL202 isogenic cells after 48 h of 50 nM talazoparib or DMSO exposure. Data representative of $n = 4$ biological replicates, error bars show \pm s.d. $**P = 0.0021$, $****P < 0.0001$, one-way ANOVA. **d**, Western blot showing expression of CINP and p21 in MEL202 isogenic cells after NTC or *CINP* gene silencing 48 h after 50 nM talazoparib exposure. Data are representative of $n = 2$ biological replicates. **e**, Western blot of pCHK2 (T68) and CINP expression in MEL202 isogenic cells after NTC or *CINP* gene silencing and 48 h of 50 nM

talazoparib or DMSO exposure. Images are representative of $n = 3$ biological replicates. **f**, Scatterplot showing the nuclear intensity of p21 in MEL202^{R625G} cells expressing control-GFP or CINP-GFP, after 48 h of 50 nM talazoparib or DMSO exposure. Data are representative of $n = 2$ biological replicates, error bars show \pm s.d. $****P < 0.0001$, one-way ANOVA. **g**, Western blot of pCHK2 (T68) and total CHK2 expression in MEL202^{R625G} cells expressing control-GFP or CINP-GFP, after 48 h of 50 nM talazoparib or DMSO exposure. Images are representative of $n = 2$ biological replicates. **h**, Box and whiskers plot showing nuclear area of MEL202 isogenic cells after 24 h and 48 h of 50 nM talazoparib or DMSO exposure. Data are mean of three biological replicates, error bars show \pm s.e.m. **i**, Box and whiskers plot depicting nuclear area of MEL202^{R625G} cells expressing control-GFP or CINP-GFP, after 48 h of 50 nM talazoparib or DMSO exposure. Data are mean of $n = 3$ biological replicates, error bars show minimum to maximum nuclear area. $****P < 0.0001$, one-way ANOVA (**h** and **i**).

was predominantly maintained after drug wash off, whereas the MEL202^{R625G-DEG} cells showed no significant response to PARPi exposure (Fig. 5a and Extended Data Fig. 9a). Further investigation quantified that the immediate accumulation of cells in G₂/M corresponds with a decrease in the G₁ population, rather than a difference in the

proportion of cells in S phase following PARPi exposure (Extended Data Fig. 9b). PARPi exposure produced a dose-dependent induction of pCHK1 (S345) in MEL202^{R625G} cells at 48 h, indicating a functional ATR/CHK1 DNA damage response, coinciding with the recruitment of 53BP1 and γ H2AX to sites of DNA damage (Extended Data Fig. 9c and

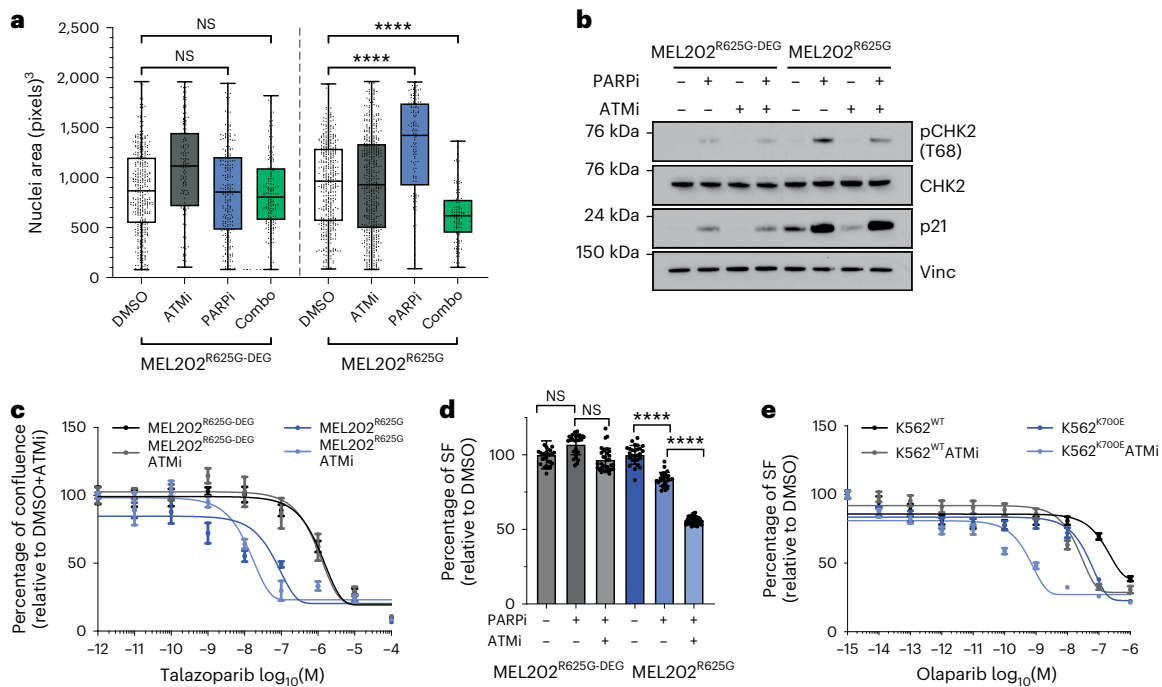


Fig. 6 | PARPi and ATMi combination treatment lower the G₂/M checkpoint. **a,b**, Box and whiskers plot showing nuclear area (**a**), and western blot of pCHK2 (T68), total CHK2 and p21 expression in MEL202 isogenic cells after 48 h of exposure with 400 nM ATMi (KU-55933), 50 nM talazoparib, combination exposure or DMSO (**b**). $n = 3$ independent biological replicates, error bars show minimum to maximum nuclear area. **** $P < 0.0001$, one-way ANOVA. **c**, Talazoparib dose–response curves of MEL202 isogenic cells treated with

DMSO or ATMi KU-55933. Data are mean of $n = 3$ biological replicates, error bars show \pm s.e.m. **d**, Column bar graph showing the relative survival of MEL202 isogenic cells after days of exposure with 50 nM talazoparib, combination with ATMi AZD0156 or DMSO. Data are mean of $n = 3$ biological replicates, error bars show \pm s.e.m. **e**, Dose–response curves of K562 isogenic cells exposed to olaparib in combination with DMSO or ATMi AZD0156. Data are mean of $n = 3$ replicates, error bars show \pm s.e.m. **** $P < 0.0001$, unpaired two-tailed t -test.

Fig. 4e,f). This paralleled with increased pATM (S1981) in MEL202^{R625G} cells, which canonically induced pCHK2 (T68) and nuclear p21 (Waf/Cip1) protein expression in both MEL202^{R625G} and K562^{K700E} cells (Fig. 2b, Fig. 5b,c and Extended Data Fig. 9d–f). This activity is reported to inhibit the kinase activity of CDK1-cyclin B, thus blocking progression through G₂/M⁴⁹. Consistent with our earlier observations, these phenotypes were also observed in MEL202^{R625G-DEG} cells upon *CINP* gene silencing (Fig. 5d,e, Extended Data Fig. 9g,h and Supplementary Fig. 5a) and could be rescued through the reexpression of CINP in MEL202^{R625G} cells (Fig. 5f,g and Supplementary Fig. 5b). Of note, PARPi exposure here did not lead to high levels of single strand or double strand DNA damage measurable by alkaline and neutral COMET assays, respectively, in either MEL202^{R625G-DEG} or MEL202^{R625G} cells (Supplementary Fig. 5c–g). This is an outcome in agreement with studies highlighting that higher levels of DSBs only occur upon progression into a subsequent cell cycle after PARPi exposure^{42,50}.

Using BIRC5 (survivin), which acts as a subunit of the chromosomal passenger complex (CPC) to regulate key mitotic events^{51,52}, to assess the mitotic phases under PARPi exposure, we observed normal mitotic progression of MEL202^{R625G-DEG} cells, whereas MEL202^{R625G} cells were entirely in interphase. MEL202^{R625G} cells showed nuclear translocation of survivin (Supplementary Fig. 5h,i), supporting the notion that survivin has a dual role as an apoptosis inhibitor and a mitotic effector, where a change from antiapoptotic to CPC function occurs in G₂/M as the cells prepare for mitosis^{51,52}. We also observed a significant reduction in the percentage of mitoses (using the marker phospho-histone H3 (S10)⁵³) in MEL202^{R625G} cells exposed to PARPi (Supplementary Fig. 5j), which was accompanied by an increase in nuclear area and pericentrin area (Fig. 5h and Supplementary Fig. 6a,b), indicative of cells at the G₂/M checkpoint⁴. This was also rescued in MEL202^{R625G} cells overexpressing CINP (Fig. 5i and Extended Data Fig. 8d–h).

These results indicate that the deficient response of *SF3B1*^{MUT} cells to the replication stress caused by PARPi exposure leads to increased fork origin firing, a subsequent increase in unresolved replication intermediates and activation of the G₂/M checkpoint. By reexpressing CINP in *SF3B1*^{MUT} cells, we can rescue the DNA damage and G₂/M checkpoint activation caused by PARP inhibition, and ultimately, the sensitivity of *SF3B1*^{MUT} cells to talazoparib (Fig. 4d and Extended Data Fig. 8i).

Given our observations that G₂/M checkpoint activation upon PARPi exposure is primarily regulated by the ataxia-telangiectasia mutated (ATM)/CHK2 pathway in *SF3B1*^{MUT} cells⁵⁴, we hypothesized that treating *SF3B1*^{MUT} cells with combinations of PARPi and ATM inhibitors (ATMi) would abrogate G₂/M stalling, leading to further cell death. In contrast to the increase in nuclear area caused by single-agent PARPi, a combination of talazoparib with the ATMi KU-55933 resulted in a significant reduction in nuclear area in MEL202^{R625G} cells compared to PARPi or DMSO (Fig. 6a). Consistent with this, we observed a reduction in pCHK2 (T68) phosphorylation with the combination of PARPi with either KU-55933 (Fig. 6b) or the more potent ATMi AZD0156 (Supplementary Fig. 6c). Finally, PARPi and ATMi combinations led to a significant reduction in the viability of both MEL202^{R625G} and K562^{K700E} cells compared to PARPi alone (Fig. 6c–e and Supplementary Fig. 6d). In contrast to this, the combination of either CHK1i or ATRi with talazoparib was not selective in MEL202^{R625G} cells (Supplementary Fig. 6e,f).

PARPi suppress *SF3B1*^{MUT} growth and metastasis in vivo

We subsequently tested the in vivo therapeutic potential of single-agent PARPi talazoparib in *SF3B1*^{MUT} cells. In both, MEL202^{R625G-DEG} and MEL202^{R625G} tumor-bearing mice that received the drug vehicle alone, tumor growth continued unabated and liver micrometastases were observed in all mice (Fig. 7a–d). In contrast, talazoparib treatment (0.33 mg kg⁻¹) had a strong antitumor effect in the MEL202^{R625G}

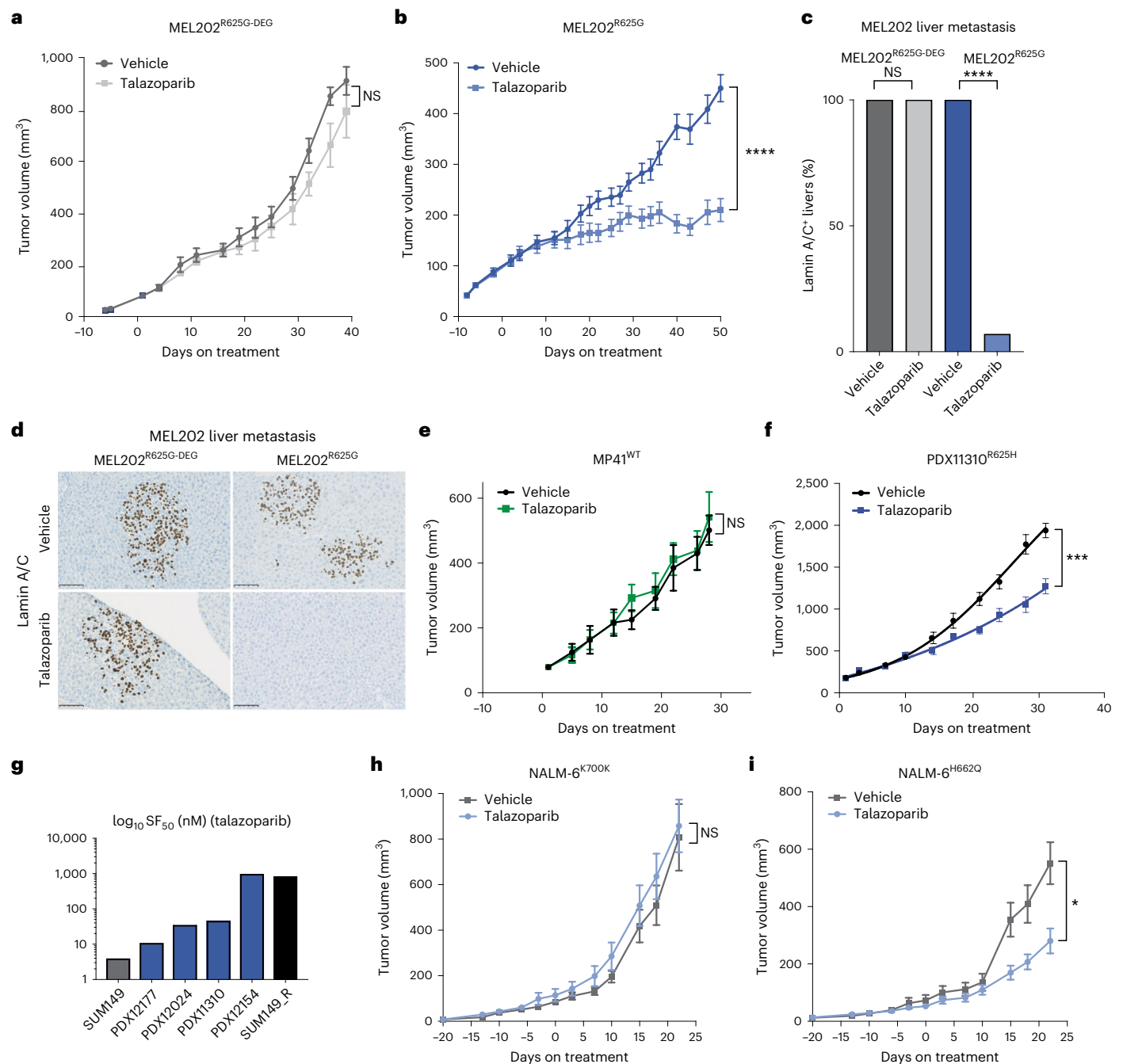


Fig. 7 | PARP inhibition suppresses *SF3B1*^{MUT} tumor growth and metastasis in vivo. **a**, Chart depicting tumor volume of the therapeutic response to talazoparib treatment in NSG-nude mice bearing MEL202^{R625G-DEG} xenograft tumors over time (0.33 mg kg⁻¹). Day 0 represents the first day of treatment. Tumors, vehicle *n* = 8, talazoparib *n* = 9. NS, *P* = 0.1825, two-way ANOVA. **b**, Chart depicting tumor volume of the therapeutic response to talazoparib treatment in NSG-nude mice bearing *SF3B1*^{MUT} MEL202^{R625G} xenograft tumors over time, (0.33 mg kg⁻¹). Day 0 represents the first day of treatment. Tumors, vehicle *n* = 16, talazoparib *n* = 15. *****P* < 0.0001, two-way ANOVA. **c**, Bar plot of number of mice with or without human lamin A/C positive cells in liver sections, representing liver metastasis of all MEL202^{R625G-DEG} and MEL202^{R625G} subcutaneous tumors under talazoparib treatment. *****P* < 0.0001, unpaired two-tailed *t*-test. **d**, Representative images of immunohistochemical assay of mouse livers from the MEL202^{R625G-DEG} and MEL202^{R625G} cells grown in vivo. Scale bar, 100 μm. **e**, **f**, Chart depicting tumor volume of the therapeutic response to talazoparib treatment in NSG-nude mice

bearing *SF3B1*^{WT} and *SF3B1*^{MUT} patient-derived xenograft tumors MP41^{WT} (**e**) and PDX11310^{R625H} (**f**) over time, (0.33 mg kg⁻¹). Day 0 represents the first day of treatment. MP41^{WT} tumors, vehicle *n* = 9, talazoparib *n* = 9. NS, *P* = 0.6536, two-way ANOVA. PDX11310^{R625H} tumors, vehicle *n* = 10, talazoparib *n* = 10. ****P* = 0.0005, two-way ANOVA. **g**, Bar plot of SF₅₀ concentrations of talazoparib efficacy in a series of *SF3B1*^{MUT} patient-derived organoids (R625C (PDX12177, PDX12024 and PDX12154), R625H (PDX11310) grown ex vivo. Three-dimensional cultures of the *BRCA1*^{MUT} SUM149 and revertant SUM149 cell lines were used as controls of PARPi sensitivity, respectively. Data are mean of *n* = 1 biological replicate and *n* = 6 technical replicates, error bars show ±s.e.m. **h**, **i**, Growth charts depicting tumor volume of the therapeutic response to talazoparib treatment of NALM-6^{K700K} *SF3B1*^{WT} tumors and NALM-6^{H662Q} *SF3B1*^{MUT} tumors over time in CB-17 mice (0.33 mg kg⁻¹). NALM-6^{K700K} *SF3B1*^{WT} tumors, vehicle *n* = 6, talazoparib *n* = 8. NS, *P* = 0.4356, two-way ANOVA. NALM-6^{H662Q} *SF3B1*^{MUT} tumors, vehicle *n* = 8, talazoparib *n* = 8. **P* = 0.0388, two-way ANOVA.

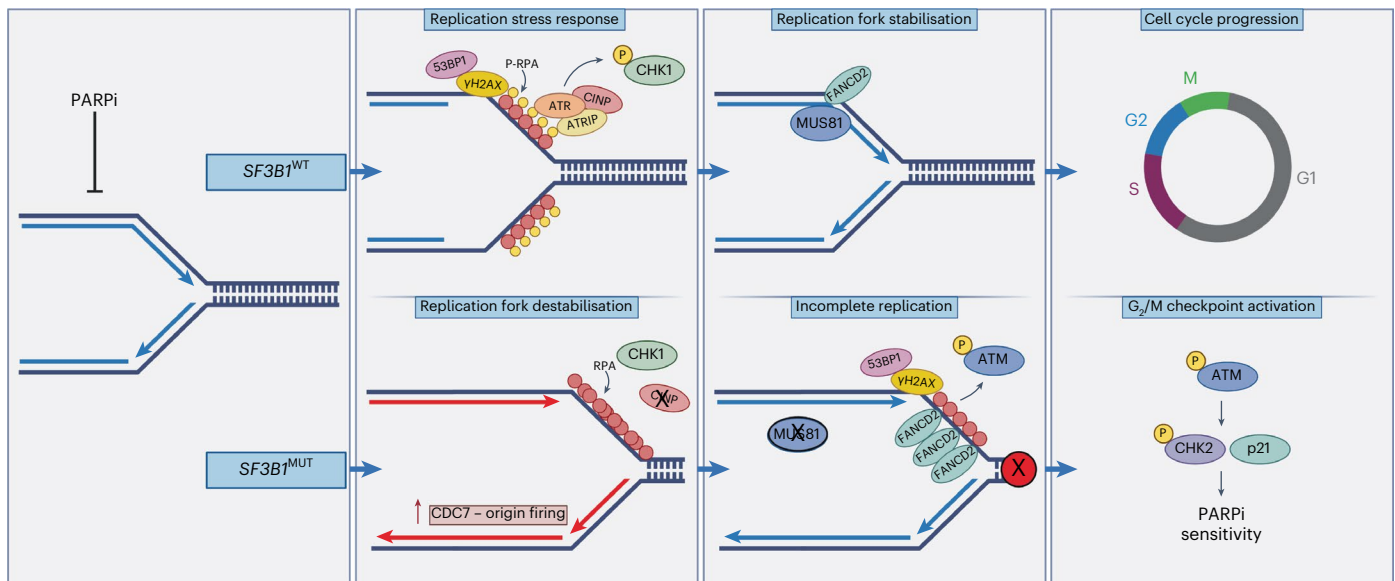


Fig. 8 | Graphical schematic of the mechanism of PARPi sensitivity in *SF3B1*^{MUT} cells. When exposed to PARPi, *SF3B1*^{MUT} cells show an impaired replication stress response (lack of pCHK1 (S317), pATR and pRPA32) due to reduced CINP protein expression. This leads to increased origin firing, unchecked fork progression

and unresolved replication intermediates via the lack of MUS81-positive FANCD2 foci. This results in ATM activation and the induction of pCHK2 (T68), stalling *SF3B1*^{MUT} cells at the G₂/M checkpoint.

tumor-bearing mice only, showed a significant reduction in their tumor volume, extended their survival, significantly prevented liver metastasis in 93% (14/15) of mice and, similar to the in vitro studies, induced pCHK2 (T68) (Fig. 7a–d, Extended Data Fig. 10a–d and Supplementary Fig. 7a–c). Cells from the *SF3B1*^{R625H} patient-derived xenograft (PDX), PDX11310, grown subcutaneously in vivo corroborated that talazoparib significantly inhibited the growth of established tumors and extended the survival of mice, whereas cells grown from the *SF3B1*^{WT} PDX, MP41, showed no significant difference in tumor volume with talazoparib treatment (Fig. 7e,f, Extended Data Fig. 10e–g and Supplementary Fig. 7d). We also observed that uveal melanoma patient-derived xenografts grown ex vivo as organoids (PDXOs), harboring R625H or R625C hotspot *SF3B1* variants, showed sensitivity to talazoparib compared to SUM149 *BRCA1*^{WT} revertant breast cancer cells⁵⁵ (Fig. 7g and Supplementary Fig. 7e). In addition, in vivo treatment of established NALM6^{H662Q} *SF3B1*^{MUT} tumors showed a significant response to talazoparib treatment compared to the vehicle; with no such antitumor effect in the NALM6^{K700K} *SF3B1*^{WT} tumors with talazoparib treatment (Fig. 7h,i and Extended Data Fig. 10h–j). Together, the effect of PARPi in this setting suggests that *SF3B1*/PARPi synthetic lethality could be further exploited and warrants investigation in future proof-of-concept clinical trials (Fig. 8).

Discussion

Mutations in spliceosomal component genes are emerging as common characteristics of human cancers. Here we show that mutations in *SF3B1* confer selective sensitivity to clinically approved PARPi, irrespective of homologous repair functionality or *BRCA1/BRCA2* status. These effects portend to multiple molecularly diverse tumor models, supporting the hypothesis that *SF3B1* mutation status, independent of genomic background, is a determinant of sensitivity to PARPi in cancer. Given that PARPi are already approved for multiple cancer types with homologous repair defects, biomarker-driven proof-of-concept trials could be instigated to assess this hypothesis in treatment-refractory patients.

Mechanistically, these data represent a paradigm shift away from the current dogma that homologous recombination defects are the only cause of PARPi sensitivity, and implicate the largely uncharacterized protein CINP, as a major player of the replication stress

response. PARP inhibition increased replication fork origin firing, resulting in accelerated fork progression in *SF3B1*^{MUT} cells, whereas *SF3B1*^{WT} cells under the same perturbation, induced a canonical replication stress response before reinstating an unaltered fork progression. Maya-Mendoza et al.⁴² previously described a mechanism by which a PARP1-p21 axis controls fork progression and upon PARP inhibition, fork acceleration and replication stress are induced, followed by RPA and a responsive ATR (pCHK1 S317) signaling. In the context of an *SF3B1* mutation, however, we show that CINP, which has been previously linked with the cells' ability to signal DNA damage, through the phosphorylation of CHK1 at S317 (ref. 38) is downregulated in multiple *SF3B1*^{MUT} models. This failed induction of pCHK1 (S317) coincided with a reduced replication stress response and increased origin firing upon PARPi exposure. Altered fork dynamics accumulated in unresolved replication intermediates with increased FANCD2 but lacked localized MUS81. Incomplete replication upon PARPi exposure in *SF3B1*^{MUT} cells suggests a role for CINP in the replication stress response. Here *SF3B1*^{MUT} cells induce ATM signaling via pCHK2 (T68) induction and likely fail to promote PLK1 (ref. 56), which ultimately stalls the cells in G₂/M. This PARPi-induced stalling of the cell cycle renders *SF3B1*^{MUT} cells additionally sensitive to ATM inhibition. Targeting G₂/M checkpoint activation increased sensitivity to PARPi exposure and has the clinical rationale of limiting persistent cells, which have been linked to transient resistant states under PARPi treatment⁵⁷.

Of note, we did not identify any mis-splicing event in *CINP* itself, mRNA downregulation or changes in protein stability that may explain CINP downregulation, although we cannot rule out pleiotropic mis-splicing events that may act in concert to regulate CINP protein levels. Hence the exact mechanism of CINP downregulation in *SF3B1*^{MUT} cells remains to be elucidated.

Here we note that our findings suggest a clinical utility for approved PARP-trapping agents outside the context of homologous repair-deficient cancers. Analysis of the recent PiCCLe multicenter phase 1 trial in relapsed leukemia highlighted that the patients harboring *SF3B1* mutations had the longest progression-free survival when treated with olaparib. Furthermore, we confirm CINP protein is downregulated in these *SF3B1*^{MUT} patients³⁹. Although the numbers in this study were small and at the time of writing no other trial

has reported the clinical efficacy of PARP inhibition in a homologous recombination-proficient population where *SF3B1* mutation status is known, these data suggest that PARPi treatment may have clinical benefit in this patient population. Additionally, given that a recent phase I clinical trial has reported no complete or partial responses in *SF3B1*^{MUT} cancers treated with H3B-8800, an oral small molecule that binds SF3B1 (ref. 29), our findings are very timely, and suggest a wider group of patients with *SF3B1*^{MUT} cancers, otherwise resistant to conventional treatments, may benefit from PARP-trapping drugs.

Online content

Any methods, additional references, Nature Portfolio reporting summaries, source data, extended data, supplementary information, acknowledgements, peer review information; details of author contributions and competing interests; and statements of data and code availability are available at <https://doi.org/10.1038/s41588-023-01460-5>.

References

- Darman, R. B. et al. Cancer-associated SF3B1 hotspot mutations induce cryptic 3' splice site selection through use of a different branch point. *Cell Rep.* **13**, 1033–1045 (2015).
- Seiler, M. et al. Somatic mutational landscape of splicing factor genes and their functional consequences across 33 cancer types. *Cell Rep.* **23**, 282–296 (2018).
- Armenia, J. et al. The long tail of oncogenic drivers in prostate cancer. *Nat. Genet.* **50**, 645–651 (2018).
- Biankin, A. V. et al. Pancreatic cancer genomes reveal aberrations in axon guidance pathway genes. *Nature* **491**, 399–405 (2012).
- Harbour, J. W. et al. Recurrent mutations at codon 625 of the splicing factor SF3B1 in uveal melanoma. *Nat. Genet.* **45**, 133–135 (2013).
- Imielinski, M. et al. Mapping the hallmarks of lung adenocarcinoma with massively parallel sequencing. *Cell* **150**, 1107–1120 (2012).
- Landau, D. A. et al. Evolution and impact of subclonal mutations in chronic lymphocytic leukemia. *Cell* **152**, 714–726 (2013).
- Maguire, S. L. et al. *SF3B1* mutations constitute a novel therapeutic target in breast cancer. *J. Pathol.* **235**, 571–580 (2015).
- Papaemmanuil, E. et al. Somatic SF3B1 mutation in myelodysplasia with ring sideroblasts. *N. Engl. J. Med.* **365**, 1384–1395 (2011).
- Yoshida, K. et al. Frequent pathway mutations of splicing machinery in myelodysplasia. *Nature* **478**, 64–69 (2011).
- Cerami, E. et al. The cBio cancer genomics portal: an open platform for exploring multidimensional cancer genomics data. *Cancer Discov.* **2**, 401–404 (2012).
- Gao, J. et al. Integrative analysis of complex cancer genomics and clinical profiles using the cBioPortal. *Sci. Signal.* **6**, pl1 (2013).
- Bamopoulos, S. A. et al. Clinical presentation and differential splicing of SRSF2, U2AF1 and SF3B1 mutations in patients with acute myeloid leukemia. *Leukemia* **34**, 2621–2634 (2020).
- Baliakas, P. et al. Recurrent mutations refine prognosis in chronic lymphocytic leukemia. *Leukemia* **29**, 329–336 (2015).
- Callens, C. et al. Molecular features of untreated breast cancer and initial metastatic event inform clinical decision-making and predict outcome: long-term results of ESOPE, a single-arm prospective multicenter study. *Genome Med.* **13**, 44 (2021).
- Pearson, A. et al. Inactivating NF1 mutations are enriched in advanced breast cancer and contribute to endocrine therapy resistance. *Clin. Cancer Res.* **26**, 608–622 (2020).
- van der Werf, I. et al. Splicing factor gene mutations in acute myeloid leukemia offer additive value if incorporated in current risk classification. *Blood Adv.* **5**, 3254–3265 (2021).
- Yavuziyigitoglu, S. et al. Uveal melanomas with SF3B1 mutations: a distinct subclass associated with late-onset metastases. *Ophthalmology* **123**, 1118–1128 (2016).
- Alsafadi, S. et al. Cancer-associated SF3B1 mutations affect alternative splicing by promoting alternative branchpoint usage. *Nat. Commun.* **7**, 10615 (2016).
- Furney, S. J. et al. SF3B1 mutations are associated with alternative splicing in uveal melanoma. *Cancer Discov.* **3**, 1122–1129 (2013).
- Kahles, A. et al. Comprehensive analysis of alternative splicing across tumors from 8,705 patients. *Cancer Cell* **34**, 211–224 (2018).
- Kesarwani, A. K. et al. Cancer-associated SF3B1 mutants recognize otherwise inaccessible cryptic 3' splice sites within RNA secondary structures. *Oncogene* **36**, 1123–1133 (2017).
- Cretu, C. et al. Molecular architecture of SF3b and structural consequences of its cancer-related mutations. *Mol. Cell* **64**, 307–319 (2016).
- Gentien, D. et al. A common alternative splicing signature is associated with SF3B1 mutations in malignancies from different cell lineages. *Leukemia* **28**, 1355–1357 (2014).
- Zhou, Q. et al. A chemical genetics approach for the functional assessment of novel cancer genes. *Cancer Res.* **75**, 1949–1958 (2015).
- Obeng, E. A. et al. Physiologic expression of Sf3b1(K700E) causes impaired erythropoiesis, aberrant splicing, and sensitivity to therapeutic spliceosome modulation. *Cancer Cell* **30**, 404–417 (2016).
- Seiler, M. et al. H3B-8800, an orally available small-molecule splicing modulator, induces lethality in spliceosome-mutant cancers. *Nat. Med.* **24**, 497–504 (2018).
- Steensma, D. P. et al. H3B-8800-G0001-101: a first in human phase I study of a splicing modulator in patients with advanced myeloid malignancies. *J. Clin. Oncol.*, https://doi.org/10.1200/jco.2017.35.15_suppl.tps7075 (2018).
- Steensma, D. P. et al. Phase I first-in-human dose escalation study of the oral SF3B1 modulator H3B-8800 in myeloid neoplasms. *Leukemia* **35**, 3542–3550 (2021).
- Inoue, D. et al. Spliceosomal disruption of the non-canonical BAF complex in cancer. *Nature* **574**, 432–436 (2019).
- Liu, Z. et al. Mutations in the RNA splicing factor SF3B1 promote tumorigenesis through MYC stabilization. *Cancer Discov.* **10**, 806–821 (2020).
- Liu, B. et al. Mutant SF3B1 promotes AKT and NF-κB driven mammary tumorigenesis. *J. Clin. Invest.* <https://doi.org/10.1172/JCI138315> (2020).
- Dalton, W. B. et al. Hotspot SF3B1 mutations induce metabolic reprogramming and vulnerability to serine deprivation. *J. Clin. Invest.* **129**, 4708–4723 (2019).
- Bajrami, I. et al. E-Cadherin/ROS1 inhibitor synthetic lethality in breast cancer. *Cancer Discov.* **8**, 498–515 (2018).
- Murai, J. et al. Trapping of PARP1 and PARP2 by clinical PARP inhibitors. *Cancer Res.* **72**, 5588–5599 (2012).
- Pettitt, S. J. et al. Genome-wide and high-density CRISPR-Cas9 screens identify point mutations in PARP1 causing PARP inhibitor resistance. *Nat. Commun.* **9**, 1849 (2018).
- Pettitt, S. J. & Lord, C. J. Dissecting PARP inhibitor resistance with functional genomics. *Curr. Opin. Genet. Dev.* **54**, 55–63 (2019).
- Lovejoy, C. A. et al. Functional genomic screens identify CINP as a genome maintenance protein. *Proc. Natl Acad. Sci. USA* **106**, 19304–19309 (2009).
- Pratt, G. et al. A multi-centre phase I trial of the PARP inhibitor olaparib in patients with relapsed chronic lymphocytic leukaemia, T-prolymphocytic leukaemia or mantle cell lymphoma. *Br. J. Haematol.* **182**, 429–433 (2018).
- Cimprich, K. A. & Cortez, D. ATR: an essential regulator of genome integrity. *Nat. Rev. Mol. Cell Biol.* **9**, 616–627 (2008).
- Gaillard, H., Garcia-Muse, T. & Aguilera, A. Replication stress and cancer. *Nat. Rev. Cancer* **15**, 276–289 (2015).

42. Maya-Mendoza, A. et al. High speed of fork progression induces DNA replication stress and genomic instability. *Nature* **559**, 279–284 (2018).
43. Wilsker, D., Petermann, E., Helleday, T. & Bunz, F. Essential function of Chk1 can be uncoupled from DNA damage checkpoint and replication control. *Proc. Natl Acad. Sci. USA* **105**, 20752–20757 (2008).
44. Bhowmick, R., Minocherhomji, S. & Hickson, I. D. RAD52 facilitates mitotic DNA synthesis following replication stress. *Mol. Cell* **64**, 1117–1126 (2016).
45. Ciccia, A., Constantinou, A. & West, S. C. Identification and characterization of the human mus81-eme1 endonuclease. *J. Biol. Chem.* **278**, 25172–25178 (2003).
46. Lemacon, D. et al. MRE11 and EXO1 nucleases degrade reversed forks and elicit MUS81-dependent fork rescue in BRCA2-deficient cells. *Nat. Commun.* **8**, 860 (2017).
47. Chen, L. et al. The augmented R-loop is a unifying mechanism for myelodysplastic syndromes induced by high-risk splicing factor mutations. *Mol. Cell* **69**, 412–425 (2018).
48. Nguyen, H. D. et al. Spliceosome mutations induce R loop-associated sensitivity to ATR inhibition in myelodysplastic syndromes. *Cancer Res.* **78**, 5363–5374 (2018).
49. Abbas, T. & Dutta, A. p21 in cancer: intricate networks and multiple activities. *Nat. Rev. Cancer* **9**, 400–414 (2009).
50. Simoneau, A., Xiong, R. & Zou, L. The *trans* cell cycle effects of PARP inhibitors underlie their selectivity toward BRCA1/2-deficient cells. *Genes Dev.* **35**, 1271–1289 (2021).
51. Mita, A. C., Mita, M. M., Nawrocki, S. T. & Giles, F. J. Survivin: key regulator of mitosis and apoptosis and novel target for cancer therapeutics. *Clin. Cancer Res.* **14**, 5000–5005 (2008).
52. Stauber, R. H., Mann, W. & Knauer, S. K. Nuclear and cytoplasmic survivin: molecular mechanism, prognostic, and therapeutic potential. *Cancer Res.* **67**, 5999–6002 (2007).
53. Angi, M. et al. Immunohistochemical assessment of mitotic count in uveal melanoma. *Acta Ophthalmol.* **89**, e155–e160 (2011).
54. Reinhardt, H. C. & Yaffe, M. B. Kinases that control the cell cycle in response to DNA damage: Chk1, Chk2, and MK2. *Curr. Opin. Cell Biol.* **21**, 245–255 (2009).
55. Drean, A. et al. Modeling therapy resistance in BRCA1/2-mutant cancers. *Mol. Cancer Ther.* **16**, 2022–2034 (2017).
56. Jaiswal, H. et al. ATM/Wip1 activities at chromatin control Plk1 re-activation to determine G2 checkpoint duration. *EMBO J.* **36**, 2161–2176 (2017).
57. Fleury, H. et al. Exploiting interconnected synthetic lethal interactions between PARP inhibition and cancer cell reversible senescence. *Nat. Commun.* **10**, 2556 (2019).

Publisher's note Springer Nature remains neutral with regard to jurisdictional claims in published maps and institutional affiliations.

Open Access This article is licensed under a Creative Commons Attribution 4.0 International License, which permits use, sharing, adaptation, distribution and reproduction in any medium or format, as long as you give appropriate credit to the original author(s) and the source, provide a link to the Creative Commons license, and indicate if changes were made. The images or other third party material in this article are included in the article's Creative Commons license, unless indicated otherwise in a credit line to the material. If material is not included in the article's Creative Commons license and your intended use is not permitted by statutory regulation or exceeds the permitted use, you will need to obtain permission directly from the copyright holder. To view a copy of this license, visit <http://creativecommons.org/licenses/by/4.0/>.

© The Author(s) 2023

¹The Breast Cancer Now Toby Robins Research Centre, The Institute of Cancer Research, London, UK. ²Division of Cancer Biology, The Institute of Cancer Research, London, UK. ³Biological Services Unit, The Institute of Cancer Research, London, UK. ⁴The Cancer Research UK Gene Function Laboratory, The Institute of Cancer Research, London, UK. ⁵University Hospitals Birmingham NHS Foundation Trust, Birmingham, UK. ⁶Institute of Cancer and Genomic Sciences, University of Birmingham, Birmingham, UK. ⁷Liverpool Ocular Oncology Research Group, Department of Molecular and Clinical Cancer Medicine, University of Liverpool, Liverpool, UK. ⁸Inserm U830, PSL University, Institut Curie, Paris, France. ⁹Present address: Stem Cells and Cancer Division, The Walter and Eliza Hall Institute of Medical Research, Melbourne, Victoria, Australia. ¹⁰Present address: Translational Cancer Metabolism Team, Centre for Tumour Biology, Barts Cancer Institute, Cancer Research UK Centre of Excellence, Queen Mary University of London, Charterhouse Square, London, UK. ✉e-mail: rachael.natrajan@icr.ac.uk

Methods

All research described complies with all relevant ethical regulations. The in vivo studies carried out at The Institute of Cancer Research were performed to ARRIVE guidelines and regulations as described in the UK Animals Scientific Procedures Act 1986 and according to the UK Home Office projected licenses held by CJL and approved by the ethics board at The Institute of Cancer Research (maximum tumor size, 15 mm diameter). Additional in vivo studies were performed to local regulatory guidelines at Institut Curie (MP41 and MEL202^{R625G-DEG}; CEEA-IC118, authorization APAFis 25870-2020060410487032-v1 given by National Authority; maximal tumor volume, 2,500 mm³) and Crown Biosciences (PDX11310; maximum tumor size, 2,000 mm³). The maximal tumor size was not exceeded. Patients that provided samples, from which PDX were generated, were appropriately and fully consented. Additional methods are detailed in Supplementary Methods (Supplementary Information).

Cell lines

K562 SF3B1^{WT}, SF3B1^{K700K}, SF3B1^{K666N}, SF3B1^{K700E}; NALM-6 SF3B1^{WT}, SF3B1^{K700K} and SF3B1^{H662Q}, SF3B1^{K700E}, SF3B1^{K666N} engineered isogenic cell lines were obtained from Horizon Discovery²⁷. K562 and NALM-6 cells were maintained in IMDM and RPMI-1640 (Gibco), respectively, supplemented with heat-inactivated FBS (Gibco) and 1% penicillin/streptomycin. MEL202 parental SF3B1^{R625G} and SF3B1^{WT} revertant cell lines (MEL202^{R625G-DEG}), and MP46^{WT}, MEL270^{WT} and MP41^{WT} patient-derived SF3B1^{WT} uveal melanoma cells⁵⁸ were cultured in RPMI-1640. MEL202^{R625G-DEG} cells were engineered using the Degron-knock-in approach to harbor a degradable tag on the SF3B1^{MUT} allele as described^{25,59}. Shield-1 powder (Takara) was dissolved in 100% ethanol at 1 mmol l⁻¹ and stored at -20 °C. Shield-1 (Takara) was added to the fresh tissue culture media immediately before usage. All cell lines were tested regularly to confirm no mycoplasma infection using the MycoalertTM Mycoplasma Detection Kit as per the manufacturer's instructions (Lonza). Cells were authenticated by short tandem repeat typing with the Geneprint10 Kit (Promega) and were sequenced to check the retention of engineered alterations during culture. Authentication testing was last performed for all cell lines in July 2022.

Small-molecule drug screen

The high-throughput small-molecule drug screen was performed as previously described⁶⁰, using an in-house curated 80 compound drug library present at concentrations (0.5, 1, 5, 10, 50, 100, 500 and 1,000 nM; Supplementary Table 1, Supplementary Methods). A total of 250 cells were seeded in each well of a series of 384-well plates. Twenty-four hours later, cells were exposed to small molecules and then continuously cultured for 5 d at which point cell viability was determined using Cell-Titer Glo (Promega). Survival fractions relative to DMSO controls for each drug concentration were calculated and LFC was plotted in GraphPad Prism v9.

Splice variant analysis by qPCR

The analysis of alternatively spliced exons was performed using 384-well plates using SYBR Green (Invitrogen), (Supplementary Information, Supplementary Methods). Primers are listed in Supplementary Table 8.

DNA-fiber analysis

For unperturbed fork dynamics, cells growing in media were incubated in medium containing 25 μM iododeoxyuridine (IdU) for 20 min, followed by 125 μM chlorodeoxyuridine (CldU) for 20 min⁶¹. To investigate the effect of talazoparib on DNA replication dynamics, cells growing in media were pre-incubated with 500 nM talazoparib ± 20 μM CDC7i (Selleckchem, XL413) for 3 h before incubation with IdU, followed by CldU. This dose of talazoparib was chosen to ensure a robust induction of replication stress, as previously described for BRCA^{WT} cells⁴².

Fork symmetry was analyzed by calculating the ratio of the leftward and rightward tracts emanating by sister forks emerging from the same replication origin; A/B ratio > 1 indicates fork asymmetry and likely increased fork stalling. To investigate replication fork progression in conditions of exogenous induction of replication stress, cells were incubated with IdU for 30 min, followed by incubation with CldU and 100 μM hydroxyurea for 1 h. Fibers were produced from 4 × 10⁵ cells, spread and stained as previously described with modifications; slides were blocked in 5% BSA-PBS for 30 min before primary antibody incubation with 1:20 mouse anti-BrdU (BD Biosciences, 347580) and 1:400 rat anti-BrdU (Abcam, ab6326). Before mounting of slides, slides were immersed in 70% ethanol, and then 100% ethanol. Slides were then imaged on a confocal microscope (Leica SP8) with ×63 oil objective. Analysis was performed with ImageJ software. A minimum of 300 fibers or 60 sister fork pairs were scored over at least three independent experiments. Tract lengths were measured inclusive of both IdU and CldU labeled tracts. To determine levels of origin firing, a minimum of 400 replication structures were scored across three independent experiments. The following structure classes were counted: ongoing forks (red-green tracts), origins (fired during IdU pulse green-red-green tracts or during CldU pulse green only tracts), terminations (red-green-red tracts), stalled forks (red only tracts) and interspersed forks (red-green-red-green tracts), and percentage of origins among all the structures was calculated in each of the experiments; data represent mean ± s.e.m. The raw data for each DNA-fiber measurement are provided in the Source Data and additional images are provided in Supplementary Fig. 1.

Immunofluorescence

Before 24 h of the drug addition, adherent cell lines were seeded on glass coverslips in a multiwell plate at a density of 50,000–100,000 cells per well. Suspension cell lines were seeded in T-25 cell culture flasks at a density of 1 × 10⁶ cells per flask and fixed in 4% paraformaldehyde in PBS for 10 min followed by three washes in PBS. Suspension cell lines were attached to glass slides using Cytospin centrifugation for 3 min at 500g following fixation. The cells were then permeabilized in 0.5% Triton X-100 in PBS followed by three washes in PBS. The cells were incubated overnight at 4 °C in the primary antibody at 1/1,000 dilution in 1.5% filtered FBS in PBS. For staining of RPA and pRPA32 foci, cells were pre-extracted in ice-cold pre-extraction buffer (10 mM HEPES pH 7.5, 300 mM sucrose, 100 mM NaCl, 1.5 mM MgCl₂ and 0.5% Triton X-100) for 2 min before fixing. The cells were washed in PBS three times and then incubated in fluorescently labeled secondary antibodies and DAPI, diluted 1/2,000 and 1/5,000, respectively, in 1.5% filtered FBS in PBS for 60 min in the absence of light. The cells were washed twice in PBS and then mounted on glass slides with Dako Fluorescence Mounting Medium (Agilent). The slides were imaged on a Leica SP8 Confocal Microscope and quantified using CellProfiler (v3.1.9). Foci were counted using the 'speckle counting' pipeline, while phospho-histone H3, Cajal Body, p21 and nuclear area analysis was performed using the 'cell/particle counting and scoring the percentage of stained objects' pipeline. Mitotic phase analysis of the MEL202^{R625G-DEG} and MEL202^{R625G} cell lines was imaged using the Zeiss Axio Observer Z1 Advanced Marianas Microscope attached with a CSU-W1 SoRa and quantified by eye. The details of antibodies and buffers used can be found in Supplementary Table 9.

Cellular viability assays

All short-term survival assays utilized 96-well cell culture plates, into which low passage, exponentially growing cells were seeded at a density of 1,000–4,000 cells per well. The drug was added 24 h post-seeding and left for 5 d of continuous exposure. Cellular viability was assessed by CellTiter-Glo luminescence assay (Promega). For clonogenic long-term assays, suspension cells were seeded in six-well plates, coated in Rat tail collagen I. NALM-6^{WT} and NALM-6^{K700K} (3,000 cells

per well), NALM-6^{H662Q} cells (3,500 cells per well); K562^{WT} (300 cells per well); K562^{K700K} and K562^{K700E} (650 cells per well). MEL202^{R625G} and MEL202^{R625G-DEG} cells were seeded in standard 6-well plates at 3,500 cells per well and SUM149 cells at 2,000 cells per well. The drug was given 24 h postseeding and to maintain a constant exposure for 14 d and fresh media with inhibitor was replaced every 72 h. For the clonogenic assay, NALM-6 and K562 cell lines were imaged without fixation and quantified on MATLAB vR20018b(9.5.0). For adherent cell lines, the colonies were solubilized with acetic acid and stained with sulphorhodamine B (Sigma-Aldrich), before measuring the optical density at 570–590 nm. Visualization of data was obtained by plotting a line of best fit to 4-parameter nonlinear regression using GraphPad Prism 9 software.

Ex vivo talazoparib efficacy studies

The efficacy of talazoparib treatment on organoid models (ex vivo, 3D Matrigel assay) for the selected PDO models, SUM149 cell lines and the subsequent PDX11310 treatment in vivo study was carried out by Crown Bioscience San Diego (Supporting Information, Supplementary Methods).

In vivo talazoparib efficacy studies

The NALM-6, MEL202^{R625G}, MEL202^{R625G-DEG} and MP41 in vivo studies were performed by injecting cells subcutaneously in PBS:Matrigel (1:1; Corning Life Sciences) into 7–8 week female CB-17 (NOD.CB17-*Prkdc*^{scid}/J)-NALM-6 and NSG-nude mice (NOD.Cg-*Foxn1*^{em1Dvs}*Prkdc*^{scid}Il2rg^{tm1Wjl}/J)-MEL202 and MP41. To assess the tumor growth rates of NALM-6^{K700K} and NALM-6^{H662Q} cell lines under talazoparib treatment in CB-17 mice, treatment was given through oral gavage, with a 5 on 2 off routine at 0.33 mg kg⁻¹. A total of 2 × 10⁷ cells were injected and when tumors averaged 100 mm³, mice were randomized and treatment commenced. For the MEL202 in vivo study, tumor growth rates and liver metastases of the MEL202 cell line with talazoparib treatment were assessed. A total of 8 × 10⁶ cells (MEL202^{R625G}) and 1 × 10⁶ cells (MEL202^{R625G-DEG}) were injected subcutaneously into NSG-Nude mice and when tumors averaged 100 mm³, mice were randomized and underwent treatment. Treatment was given through oral gavage, daily, at a concentration of 0.33 mg kg⁻¹. For both studies, the Solutol-based vehicle was 10% DMAC, 6% Solutol and 84% PBS, DMSO controls were also diluted in the vehicle, tumors were measured 2/3 times a week with calipers and mice were weighed twice a week. Studies were terminated when control arm measurements neared but were less than 15 mm in diameter, in any direction, and statistical analysis was performed using Prism. The PDX model MP41 was treated with the PARPi talazoparib in vivo at the Institut Curie. Tumor fragments of 15 mm³ were transplanted into NSG-nude mice and animals were randomized when the tumor volume reached 100 mm³ and treated with vehicle (10% DMAC, 6% Solutol and 84% PBS; Group 1) or talazoparib (0.33 mg kg⁻¹; Group 2) and approved by local ethics. Groups 1 and 2 were killed on day 28. The PDX model PDX11310 was treated with the PARPi talazoparib in vivo in 7- to 8-week-old female NOD-SCID (NOD.Cg-*Prkdc*^{scid}/J) mice by Crown Bioscience. Animals were randomized when the tumor volume reached 150–250 mm³ and treated with vehicle (Group 1; 10% DMAC, 6% Solutol and 84% PBS) or talazoparib (0.33 mg kg⁻¹; Group 2) and approved by local ethics. Groups 1 and 2 were euthanized on day 31. End-of-study tumors were taken for fixed and snap-frozen samples. Tumor cDNA and gDNA from each animal were taken and sequenced to check for the retention of the SF3B1^{R625H} variant, originally denoted in this PDX model. Tumors were formalin-fixed and paraffin-embedded (FFPE), and sections were stained with hematoxylin and eosin (H&E), or incubated with antibodies against Ki-67 and cleaved caspase-3.

Cell cycle analysis

Cell cycle analysis was undertaken using propidium iodide (Abcam, ab14083) and analyzed on BD LSRII cell analyzer. Trypsinized cells

were washed twice in PBS before fixation through the dropwise addition of 70% ethanol and allowed to fix for 30 min at 4 °C. Cell pellets were washed twice with PBS at 850g, treated with 50 μl of 100 μg ml⁻¹ RNase and resuspended in 200 μl of 50 μg ml⁻¹ propidium iodide. Forward and side scatters were set to identify single cells and doublets were excluded. Gates were then automatically set and percentages were derived by use of FlowJO v10.8 (BD Biosciences) analysis software.

Cell cycle reporter cell lines, MEL202^{R625G} and MEL202^{R625G-DEG} were generated with the Incucyte Cell Cycle Green/Red Lentivirus Reagent (EF1α-Puro; Satorius 4779), at an MOI of 0.03 transduction units (TU) per cell, and cultured in 2 μg ml⁻¹ puromycin (Gibco) for 21 days to isolate and amplify stable clones. Stably transfected cells were plated in 12-well plates at a density of 100,000 cells per well. Twenty-four hours post seeding, cells were treated with talazoparib and imaged at 1 h intervals on the Incucyte S3 Live-Cell Analysis System (Sartorius). Red, green and yellow fluorescent cells were quantified using the built-in analysis to calculate the cell cycle profile.

Paired-end RNA sequencing

RNA sequencing of K562 SF3B1^{WT} and SF3B1^{K700E} cell lines was performed using 100 ng of ribosomal-depleted RNA from cell lines grown in triplicate from independent passages and treated with 100 nM talazoparib for 48 h. RNA libraries were prepared using the NEBNext Ultra Directional RNA Library Preparation Kit according to the manufacturer's instructions, with 200 bp fragments size selection and eight cycles of PCR amplification, and were sequenced on a single lane of a HiSeq 2500 using SBS v3 chemistry (Illumina; 2 × 100 bp cycles), resulting in >40 million paired end-reads. RNA sequencing FASTQ files were aligned to the human genome (hg38) using STAR v2.5.1b⁶² with the additional custom parameters '--twopassMode Basic --outSAMstrandField intronMotif --outSAMattributes NH HI AS nM NM XS' with transcript annotations obtained from GENCODE v22. Differential gene expression analysis was performed using a negative binomial generalized log-linear model (glmQLFit and glmQLFTest) implemented in edgeR v3.34.0 (ref. 63). Normalization factors to correct for variable sequencing depth and composition bias were calculated using the trimmed mean of M-values (TMM) method⁶⁴ (calcNormFactors). GSEA was performed with FGSEA⁶⁵ v1.4.1 using the c2.cp.reactome gene sets obtained from the Broad Institute with the minimum pathway size set to 10. Genes were ranked according to $-\log_{10}(\text{raw } P \text{ value})$ multiplied by the sign of the log₂ fold change. Quantification of PSI (Ψ) (percentage spliced in) values for the alternative splicing event types (alternative 5', alternative 3', exon skip, multiple exon skip and intron retention) was performed with spladder (development version dated 3 July 2018)⁶⁶ under default settings (confidence level = 3). Additional filtering required at least five supporting and excluding junction reads in at least 25% of samples to remove under-represented events. rMATS v4.1.2 (ref. 67) was run under default parameters. Detection of differential alternative splicing events from both spladder and rMATS between K562 SF3B1^{WT} and SF3B1^{K700E} cells was assessed by performing a differential PSI (Ψ) analysis using the limma v3.48.3 package⁶⁸, Benjamini–Hochberg adjusted $P < 0.1$. Sequence motif logos illustrating 30 bp upstream and 3 bp downstream of significant alternative 3' acceptor splice sites were generated using ggseqlogo v0.1 (ref. 69). For visualization purposes, the most significant events (Benjamini–Hochberg adjusted $P < 0.01$ and $|\Delta\Psi| > 5\%$) were selected. Raw RNA-sequencing data are publicly available through SRA accession number PRJNA968072.

Total mass spectrometry and proteomic profiling

Cell lines were treated with DMSO or talazoparib at 50 nM for 48 h and cell pellets were lysed in 5% SDS per 100 mM TEAB buffer with probe sonication and heating at 95 °C. Further, 57 μg of protein was reduced with TCEP and alkylated by iodoacetamide followed by TCA (trichloroacetic acid) precipitation and digested overnight in Trypsin at 37 °C

(MS grade, Thermo Fisher) was added at 1:25 (trypsin:proteins). Peptides were TMT labeled as instructed by the manufacturer, then mixed, SpeedVac dried and fractionated on a BEHXBridge C18 column (2.1 mm i.d. × 150 mm) with a 35 min gradient from 5–35% CH₃CN/NH₄OH at pH 10. A total of 36 fractions were collected and SpeedVac dried, then resuspended in 0.5%FA/H₂O, and 50% was injected for LC–MS/MS analysis on an Orbitrap Fusion Lumos coupled with an Ultimate 3000 RSLCnano System.

Samples were loaded on a nanotrap (100 μm id × 2 cm; PepMap C18, 5 μm) at 10 μl min⁻¹ with 0.1% formic acid and then separated on an analytical column (75 μm id × 50 cm; PepMap C18, 2 μm) over at 300 nl min⁻¹ at a 90 min gradient of 4–30.4% CH₃CN/0.1% formic acid per 120 min cycle time per fraction.

Raw files were processed with Proteome Discoverer 2.3 (Thermo Fisher) and searched using both SequestHT and Mascot (v2.3 MatrixScience) against UniProt Human Reference Proteome database (January 2018) concatenated with the cRAP contaminant sequences (precursor mass tolerance, $t = 30$ ppm; fragment ion mass tolerance, 0.5 Da). Spectra were searched for fully tryptic peptides with a maximum of two miss-cleavages. Target/decoy peptides were processed with Percolator and the consensus search result was filtered to a protein false discovery rate adjusted (FDR) of 0.01 (strict) and 0.05 (relaxed). The TMT10plex reporter ion quantifier used 20 ppm integration tolerance on the most confident centroid peak at the MS3 level. Only unique peptides with average reported S/N > 3 were used for quantification. Only master proteins for each peptide group were reported.

RNA polymerase II ChIP–sequencing

K562 isogenic cell lines were submitted to Active Motif for ChIP–seq for total RNA Pol II using 30 μg input chromatin (RNA Pol II antibody Active Motif 39097). The 75-nt sequence reads generated by Illumina sequencing (using NextSeq 500) were mapped to the hg38 reference genome using BWA algorithm vv0.7.12 with default settings. Only reads passing Illumina's purity filter, aligned with no more than two mismatches and mapped uniquely to the genome were used. Peaks were called using SICER v1.1 (ref. 70) FDR of 1×10^{-10} with a gap parameter of 600 bp. Peak filtering was performed by removing false ChIP–seq peaks as defined within the ENCODE blacklist⁷¹. Merged regions were computed (genomic regions containing 1 or multiple overlapping intervals) to allow comparisons between samples. Peak ratios of the intersect of LFC > |1| K700E versus wild-type and LFC > |1| K700E versus K700K were considered differential.

Statistical analyses

Statistical analysis was carried out using R 3.5.0 (www.r-project.org) and GraphPad Prism 9. Comparisons between groups of continuous variables were made using an unpaired two-tailed Student's *t*-test, Mann–Whitney *U* test, Welch's *t*-test or ANOVA. Univariate differences in survival were analyzed by the Kaplan–Meier method and significance was determined by the log-rank test. All tests were two-sided and a *P* value of less than 0.05 was considered significant. FDR *P* values for multiple testing were used for RNA-sequencing and proteomic analyses, with an FDR value of <0.1 considered significant (unless otherwise indicated). Pathway enrichment of the proteomic data was performed with GSEA v1.18.0 (ref. 72), on a preranked list of genes sorted by their PARPi versus DMSO log₂ fold change. The number of permutations was set to 10,000 and the adjusted (FDR) *P* value cut-off was set to 0.05. The numbers of independent biological replicates are included in each figure legend as are details of the numbers of events counted. No animals were excluded from the in vivo analyses. Tumor volume data points from in vivo studies were excluded on the rare occasion the measurements were inaccurate (that is, the mice had skin thickening over the inoculation site or was not measurable on that day) as detailed in the Source Data. No data points were excluded from other experiments.

Reporting summary

Further information on research design is available in the Nature Portfolio Reporting Summary linked to this article.

Data availability

The data that support the findings of this study are available in the Supporting Information. The RNA sequencing data have been deposited in NCBI Sequence Read Archive (SRA) under accession number PRJNA968072; ChIP–seq data PRJNA968071 and the mass spectrometry proteomics data have been deposited to the ProteomeXchange Consortium via the PRIDE partner repository with the dataset identifier PXD019046. SF3B1 mutations were collated from cBioPortal <https://www.cbioportal.org/> querying MSK-IMPACT PanCancer Clinical Sequencing cohort and TCGA Pan-Cancer Atlas studies. Database access July 2020. UniProt Human Reference Proteome database (January 2018) was used as a reference for the mass spectrometry data. Source data are provided with this paper.

References

- Amirouchene-Angelozzi, N. et al. Establishment of novel cell lines recapitulating the genetic landscape of uveal melanoma and preclinical validation of mTOR as a therapeutic target. *Mol. Oncol.* **8**, 1508–1520 (2014).
- Bigot, J. et al. Splicing patterns in SF3B1 mutated uveal melanoma generate shared immunogenic tumor-specific neo-epitopes. *Cancer Discov.* <https://doi.org/10.1158/2159-8290.CD-20-0555> (2021).
- Holme, H. et al. Chemosensitivity profiling of osteosarcoma tumour cell lines identifies a model of BRCAness. *Sci. Rep.* **8**, 10614 (2018).
- Schwab, R. A. et al. The Fanconi anemia pathway maintains genome stability by coordinating replication and transcription. *Mol. Cell* **60**, 351–361 (2015).
- Dobin, A. et al. STAR: ultrafast universal RNA-seq aligner. *Bioinformatics* **29**, 15–21 (2013).
- Robinson, M. D., McCarthy, D. J. & Smyth, G. K. edgeR: a Bioconductor package for differential expression analysis of digital gene expression data. *Bioinformatics* **26**, 139–140 (2010).
- Robinson, M. D. & Oshlack, A. A scaling normalization method for differential expression analysis of RNA-seq data. *Genome Biol.* **11**, R25 (2010).
- Korotkevich, G. et al. Fast gene set enrichment analysis. Preprint at *bioRxiv* <https://doi.org/10.1101/060012> (2021).
- Kahles, A., Ong, C. S., Zhong, Y. & Ratsch, G. SplAdder: identification, quantification and testing of alternative splicing events from RNA-seq data. *Bioinformatics* **32**, 1840–1847 (2016).
- Shen, S. et al. rMATS: robust and flexible detection of differential alternative splicing from replicate RNA-seq data. *Proc. Natl Acad. Sci. USA* **111**, E5593–E5601 (2014).
- Ritchie, M. E. et al. Limma powers differential expression analyses for RNA-sequencing and microarray studies. *Nucleic Acids Res.* **43**, e47 (2015).
- Wagih, O. ggseqlogo: a versatile R package for drawing sequence logos. *Bioinformatics* **33**, 3645–3647 (2017).
- Zang, C. et al. A clustering approach for identification of enriched domains from histone modification ChIP–seq data. *Bioinformatics* **25**, 1952–1958 (2009).
- ENCODE Project Consortium An integrated encyclopedia of DNA elements in the human genome. *Nature* **489**, 57–74 (2012).
- Subramanian, A. et al. Gene set enrichment analysis: a knowledge-based approach for interpreting genome-wide expression profiles. *Proc. Natl Acad. Sci. USA* **102**, 15545–15550 (2005).

Acknowledgements

This study was supported by Breast Cancer Now as part of program funding to the Breast Cancer Now Toby Robins Research Centre (to R.N. and C.J.L.); The Institute of Cancer Research (to R.N.); and MRC Confidence in Concept award (MC_PC_16047 to R.N.); CRUK programmatic funding (to C.J.L.), CRUK program grant (C20807/A28640 to T.S. and C.O.); ICR intramural grant and Cancer Research UK program (A24881 to W.N.); Wellcome Trust 20839 (to J.C.). A.H. is supported by Site de Recherche Intégrée sur le Cancer (SiRIC2) de l'Institut Curie. The authors thank S. Dayot for generating the MEL202^{R625G-DEG} cell line. We thank V. Pena, I. Bajrami, J. Frankum, D. Krastev, F.-F. Song and D. Zatreanu for helpful discussions. We thank D. Didier and F. Nemati for help with the in vivo efficacy studies of UM models. The results shown here are in part based on data generated by the TCGA Research Network (<http://cancergenome.nih.gov/>). We acknowledge NHS funding to the ICR/Royal Marsden Hospital Biomedical Research Centre. Figs. 1c, 8 and Extended Data Fig. 1i were created with BioRender.com.

Author contributions

P.B., H.S., P.T.W., L.C., G.M., J.N., N.R., M.B.J., S.H., H.E.B., J.W., L.Y., I.M., A.R., B.P., M.A., P.G., H.P., A.G., S.N., F.N., N.G., I.R., G.P., C.O., T.S., S.B., H.K., S.E.C., R.B., S.A., A.H., M.H.S., S.P., J.C., S.H., W.N., C.J.L. and R.N. generated and analyzed data and/or developed methodology. P.B., H.S. and R.N. drafted the manuscript. All authors edited and approved the final submitted manuscript. P.B. and R.N. conceptualized the study. S.H., J.C., W.N., C.J.L. and R.N. helped in supervision and funding acquisition of the study.

Competing interests

W.N. is a named inventor on a patent describing the use of EXD2 inhibitors and stands to gain from their development as part of the ICR 'Rewards to Inventors' scheme, and was a consultant for MNM Bioscience. C.J.L. makes the following disclosures: receives and/or

has received research funding from AstraZeneca, Merck KGaA, and Artios; received consultancy from SAB membership or honoraria payments from Syncona, Sun Pharma, Gerson Lehrman Group, Merck KGaA, Vertex, AstraZeneca, Tango, 3rd Rock, Ono Pharma, Artios, Abingworth, Tesselate and Dark Blue Therapeutics; has stock in Tango, Ovibio, Enedra Tx., Hysplex and Tesselate. C.J.L. is also a named inventor on patents describing the use of DNA repair inhibitors and stands to gain from their development and use as part of the ICR 'Rewards to Inventors' scheme and also reports benefits from this scheme associated with patents for PARPi paid into CJL's personal account and research accounts at the Institute of Cancer Research. R.N. receives and/or has received academic research funding from Pfizer in the form of the Breast Cancer Now Catalyst academic grant scheme. AstraZeneca partially supported the PICCLE clinical trial (supplied by Olaparib; this study is published). The remaining authors declare no conflicts of interest.

Additional information

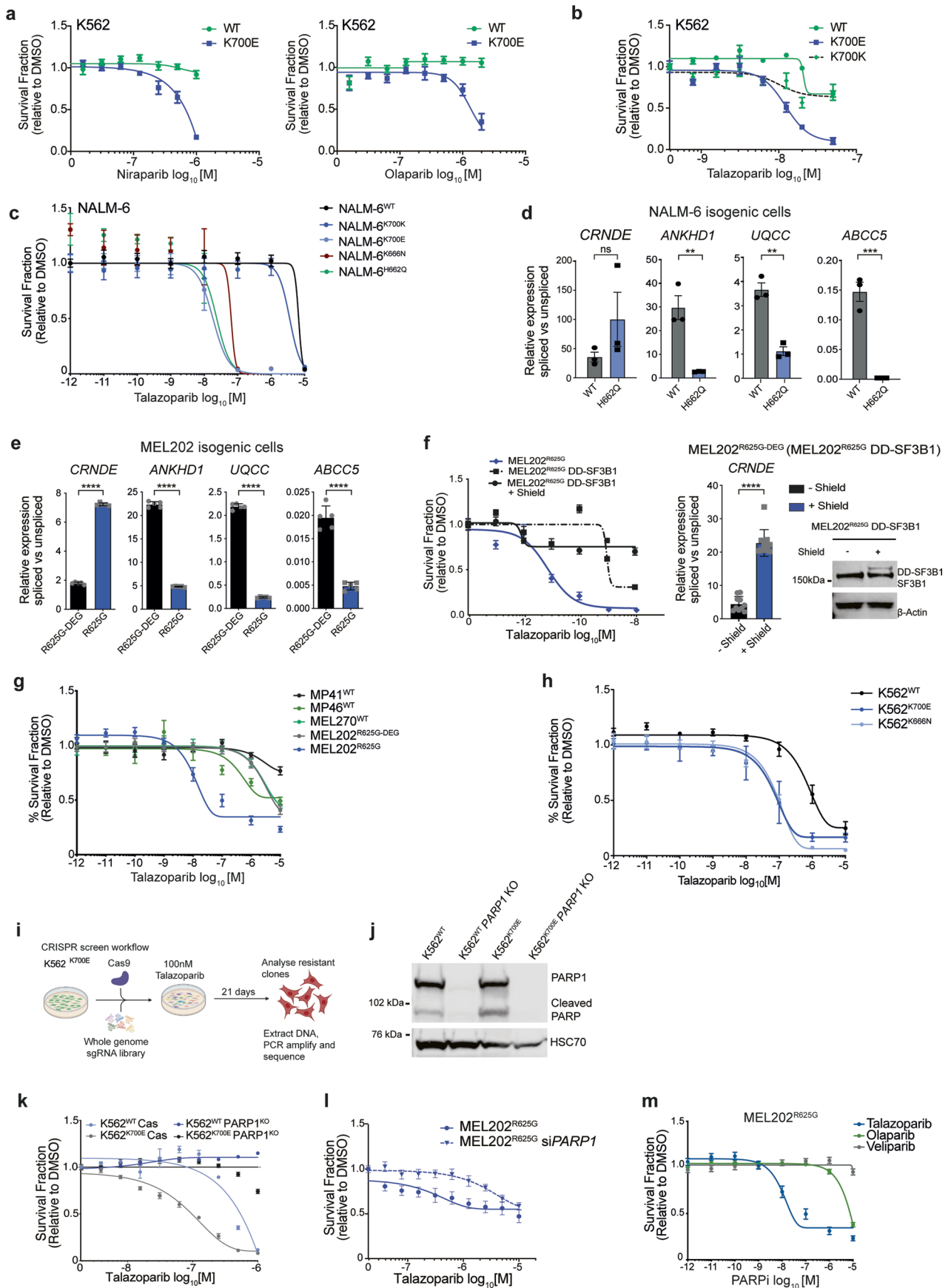
Extended data is available for this paper at <https://doi.org/10.1038/s41588-023-01460-5>.

Supplementary information The online version contains supplementary material available at <https://doi.org/10.1038/s41588-023-01460-5>.

Correspondence and requests for materials should be addressed to Rachael Natrajan.

Peer review information *Nature Genetics* thanks the anonymous reviewers for their contribution to the peer review of this work. Peer reviewer reports are available.

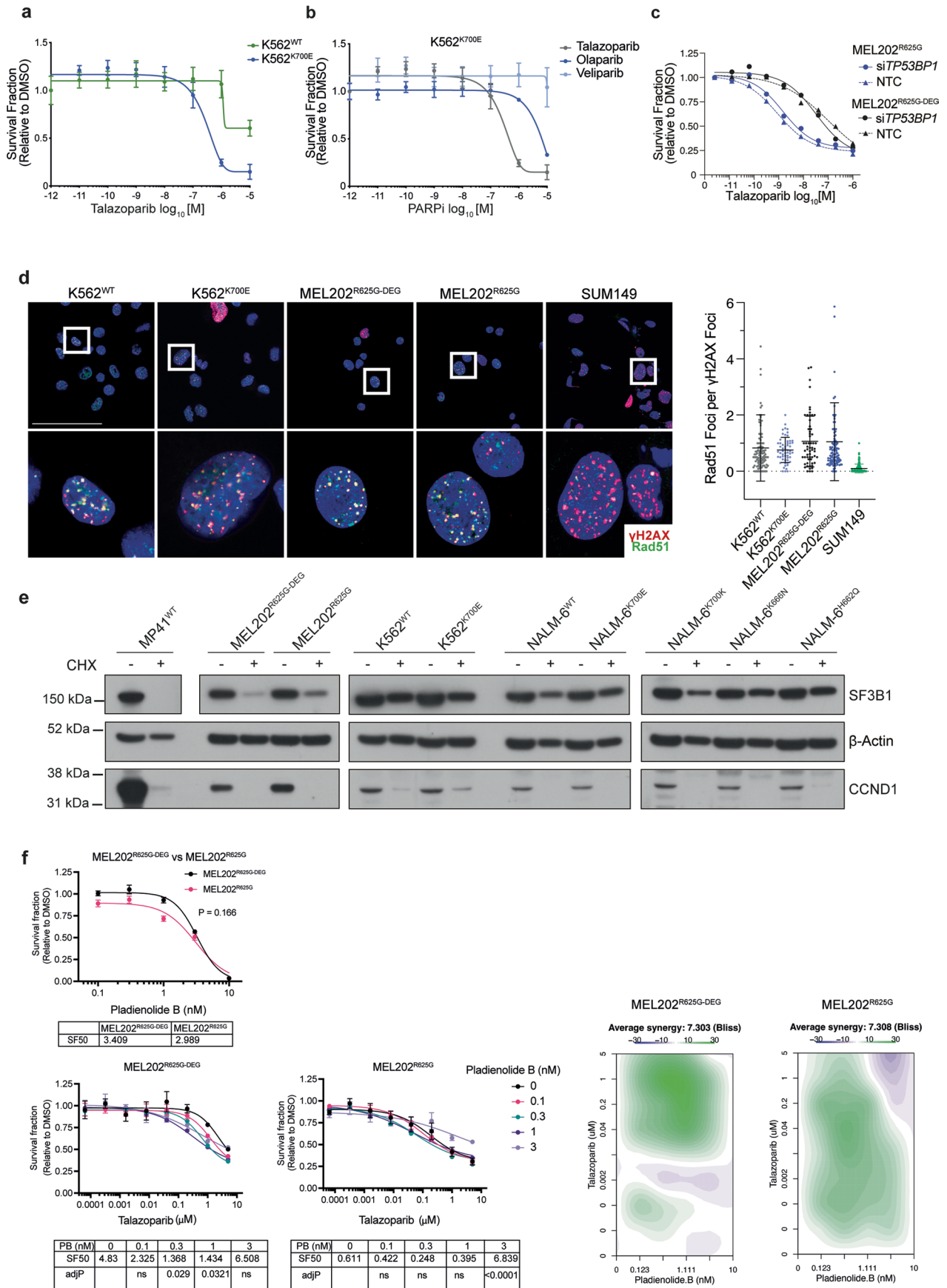
Reprints and permissions information is available at www.nature.com/reprints.



Extended Data Fig. 1 | See next page for caption.

Extended Data Fig. 1 | SF3B1 hotspot mutations induce mis-splicing and PARPi sensitivity. **a, b**, 14 day clonogenic dose–response curves of K562 SF3B1^{WT}, SF3B1^{K700K} (silent mutation) and SF3B1^{K700E} isogenic cells following exposure with distinct PARP inhibitors. Data are mean ± s.e.m. ($n = 3$ independent biological replicates). **c**, 14 day (3D viability) talazoparib dose–response curves of NALM6^{WT}, NALM6^{K700K} and SF3B1^{MUT} NALM6^{K700E}, NALM6^{K666N} and NALM6^{H662Q} cell lines grown as spheroids. Data are mean ± s.e.m. ($n = 3$ independent biological replicates). **d**, Representative qRT-PCR of differentially spliced exons of indicator genes in the NALM-6^{WT} and NALM-6^{H662Q} isogenic lines. Data are mean of $n = 3$ biological replicates, ± s.d. (unpaired two-tailed t-test (NS $P = 0.2426$, ** $P = 0.0058$, ** $P = 0.0015$, *** $P = 0.0009$)). **e**, Representative qRT-PCR of differentially spliced exons of indicator genes in the MEL202^{R625G-DEG} and MEL202^{R625G} cells. Data are mean of $n = 5$ biological replicates, ± s.d. (unpaired two-tailed t-test (**** $P < 0.0001$)). **f**, 14 day clonogenic dose–response for the isogenic MEL202^{R625G-DEG} and MEL202^{R625G} cells exposed to talazoparib and revertant MEL202^{R625G-DEG} cells labeled with a degron tag (MEL202^{R625G} DD-SF3B1) +/- Shield-1 compound to stabilize expression of the mutant allele. Data are

normalized to DMSO control and presented as mean ± s.e.m. ($n = 3$ biological replicates). qRT-PCR of differentially spliced exon of *CRNDE* in the MEL202^{R625G-DEG} +/- shield compound ($n = 3$ biological replicates, **** $P < 0.0001$, unpaired two-tail t-test). Western blot analysis of MEL202^{R625G-DEG} (MEL202^{R625G} DD-SF3B1) showing protectable mutant allele upon shield compound treatment. **g**, 5-day viability dose–response curves of wild-type uveal melanoma cell lines MP41, MP46, MEL270 and MEL202. Data are mean ± s.e.m. ($n = 3$ biological replicates). **h**, 14 day (3D viability) dose–response curves of K562^{WT}, K562^{K700E} and K562^{K666N} spheroids exposed to talazoparib. Data are mean ± s.d. ($n = 3$ independent biological replicates). **i**, Schematic of CRISPR screen workflow. **j**, Western blot of PARP1, cleaved PARP1 and HSC70 in K562^{WT} and K562^{K700E} cells with Cas or PARP1 KO. **k–l**, Talazoparib dose–response curves showing the survival fraction of K562 isogenic cells +/- PARP1 CRISPR knockout (KO) (k), MEL202^{R625G} cells +/- PARPi siRNA (l). Data are mean of $n = 3$ biological replicates, ± s.e.m. **m**, 5 day dose–response curve of MEL202^{R625G} cells exposed to talazoparib, olaparib and veliparib. Data are mean ± s.e.m. ($n = 3$ biological replicates).

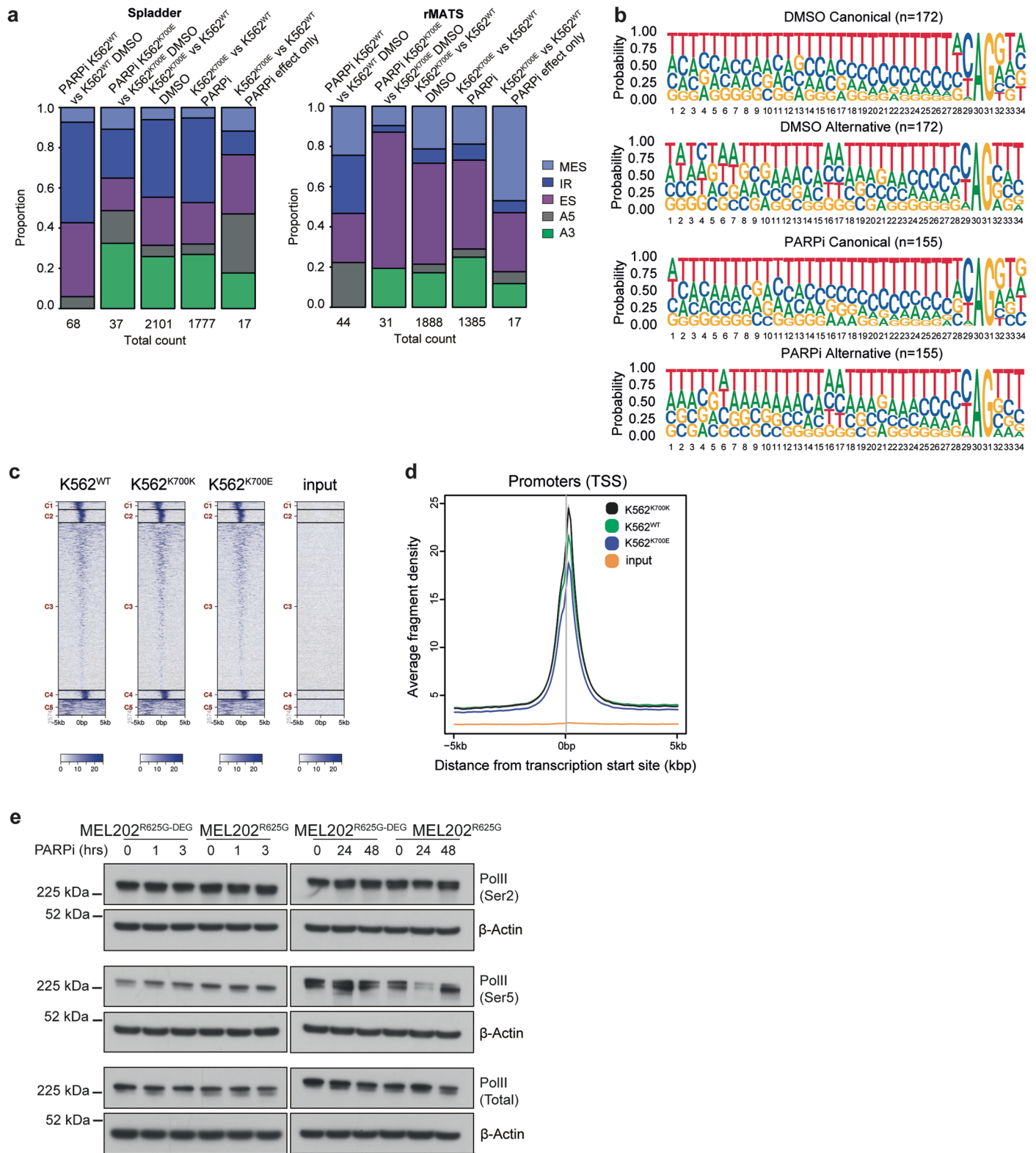


Extended Data Fig. 2 | See next page for caption.

Extended Data Fig. 2 | SF3B1 hotspot mutations induce PARPi sensitivity.

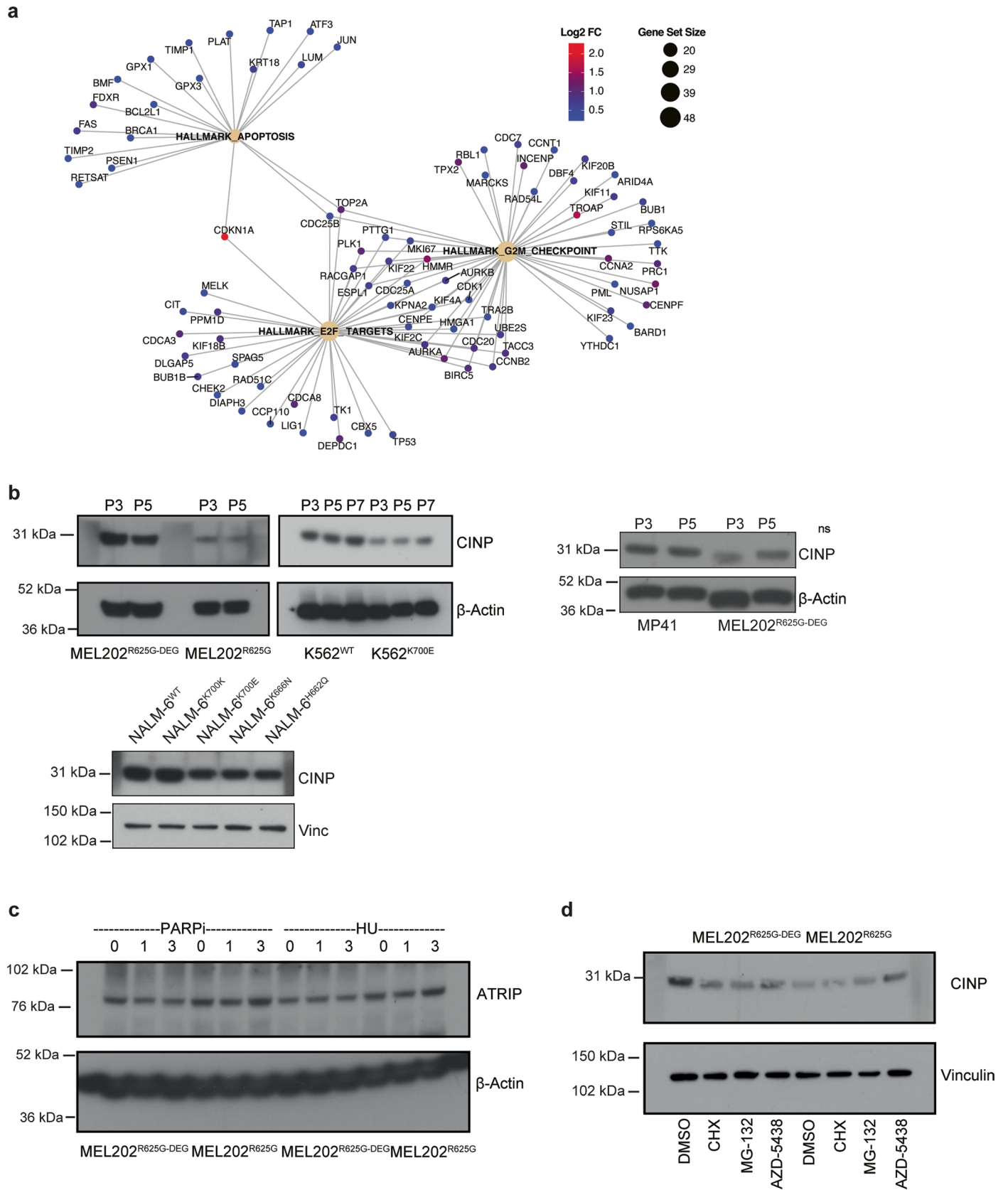
a, 5 day dose–response curve of K562^{WT} and K562^{K700E} cells treated with talazoparib ($n = 3$ biological replicates). Data are presented as mean \pm s.e.m. **b**, 5 day dose–response curve of K562^{R625G} cells exposed to talazoparib, olaparib and veliparib indicating sensitivity to more potent PARP trapping agents. ($n = 3$ biological replicates). Data are presented as mean \pm s.e.m. **c**, 5 day dose–response curve of MEL202^{R625G} cells exposed to talazoparib MEL202 isogenic cells +/- *TP53BP1* siRNA gene silencing. Data are presented as mean \pm s.e.m. ($n = 3$ technical replicates). **d**, Representative immunofluorescence images and corresponding scatter plot graph showing the number of RAD51 foci per γ H2AX foci in K562 and MEL202 isogenic cell lines and SUM149 *BRCA1*^{MUT} cells after 10 Gy irradiation. Data are presented as mean \pm s.e.m. ($n = 1$ biological replicate).

e, Western blot of SF3B1 protein expression in UM MP41^{WT} cells, MEL202, K562 and NALM-6 isogenic cell lines exposed to 50 mg/ml cycloheximide (CHX) for 48 hours. CCND1 is used as a control for protein degradation, due to a relative short half-life. **f**, Dose–response curves of MEL202^{R625G-DEG} and MEL202^{R625G} cells exposed to Pladienolide B as single agent (a) or in combination with talazoparib (b). SF50 values of combinations at different Pladienolide B concentrations are shown. Data are presented as mean, \pm s.d. of $n = 3$ technical replicates. (c) Heatmaps showing BLISS synergy scores based on the survival fraction, relative to DMSO, of MEL202 isogenic cells after 5 days of exposure to talazoparib in combination with Pladienolide B. P values from one way ANOVA with Tukey's multiple comparison test.



Extended Data Fig. 3 | *SF3B1* mutant cells show transcriptional dysregulation following PARPi exposure. **a**, Frequency plot of proportion of PSI events of aberrant splicing calculated from total RNA-sequencing ($n = 3$ biological replicates) of K562^{WT} versus K562^{K700E}, with and without PARPi (a, Spladder and b, rMATS). Multiple skipped exons (MES), retained intron (IR), skipped exon (ES), alternative 5' splice site (A5) and alternative 3' splice site (A3) events with an FDR < 0.1. **b**, Splice site motif analysis of aberrant A3 events depicting canonical and alternative branch point usage in K562^{K700E} versus K562^{WT} cells +/- talazoparib detected from total RNA sequencing. AG represents the 3'ss and the

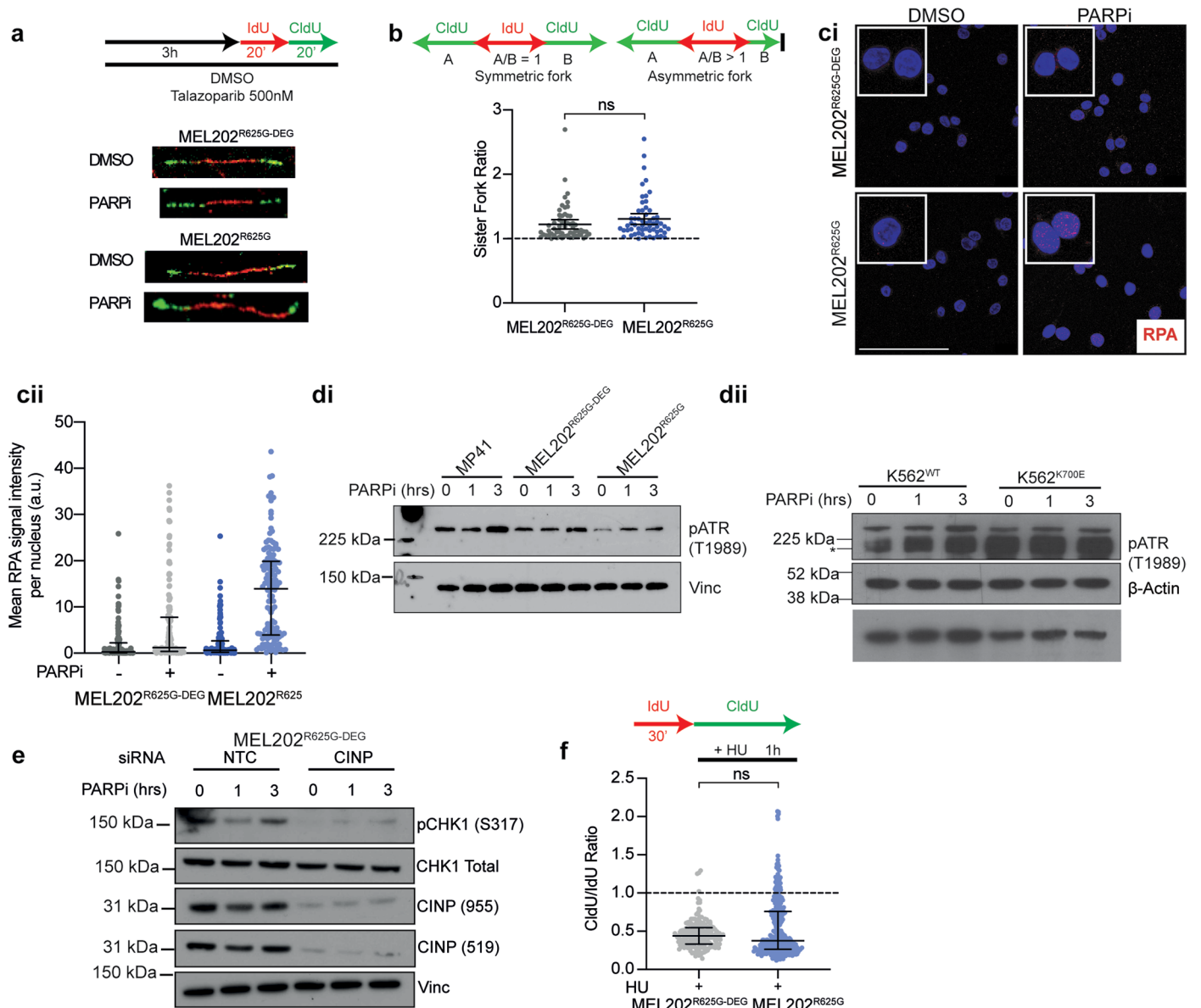
upstream adenines (A) represent the branch points. Related to Fig. 2a. **c**, Heatmap depicting the distribution of the overall binding of RNA Pol II in K562^{WT}, K562^{K700K} control and K562^{K700E} cells. **d**, Frequency plot of RNA Pol II binding at transcription start sites in the K562^{WT}, K562^{K700K} control and K562^{K700E} cells. ($n = 1$ biological replicate). **e**, Western blot of Ser5 (initiation), Ser2 (elongation) and total RNA Pol II in MEL202^{R625G-DEG} and MEL202^{R625G} cells exposed to short term (0, 1, 3 hours) and long term (0, 24 and 48 hours) talazoparib alongside β-Actin loading control ($n = 1$ biological replicate).



Extended Data Fig. 4 | See next page for caption.

Extended Data Fig. 4 | G₂/M checkpoint protein expression in *SF3B1* mutant cells under PARPi. **a**, Schematic showing the log₂FC of protein expression in the gene sets 'HALLMARK_APOPTOSIS', 'HALLMARK_E2F_TARGETS', and 'HALLMARK_G2M_CHECKPOINT', and the overlapping genes in these gene sets. Data taken from the total-MS (mass spectrometry) in Fig. 2d. **b**, Western blot of CINP and β-Actin loading control in MEL202, K562 and NALM-6 *SF3B1*^{WT} and *SF3B1*^{MUT} isogenic cell line pairs under different cell passages ('P'). **c**, Western

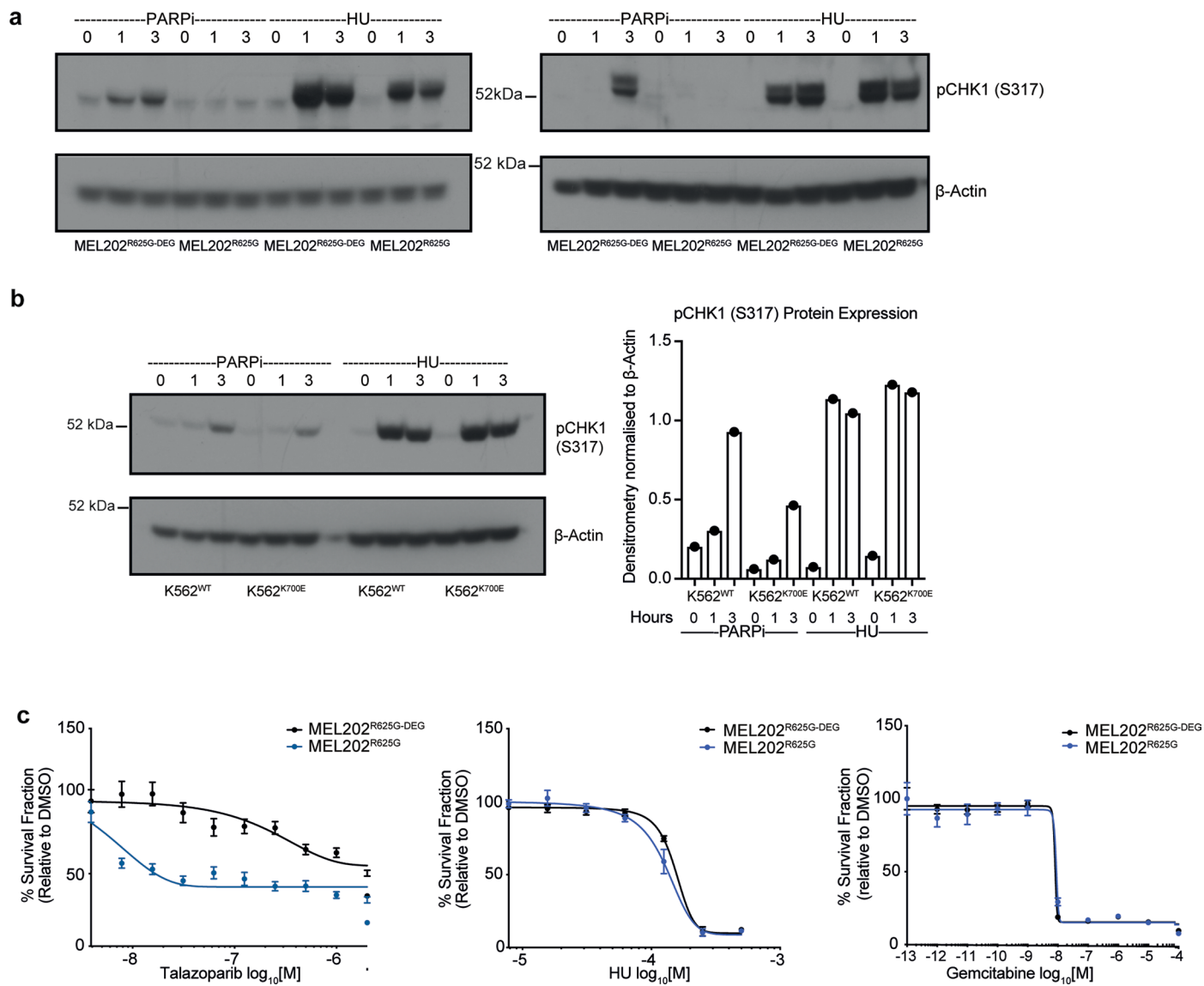
blot of total ATRIP and β-Actin loading control in MEL202, *SF3B1*^{WT} and *SF3B1*^{MUT} isogenic cell lines +/- PARPi talazoparib or hydroxyurea (HU) for indicated times (hours) (*n* = 1 biological replicate). **d**, Western blot of CINP expression in MEL202^{R625G-DEG} and MEL202^{R625G} cells and vinculin loading control after 6 hours exposure to DMSO, cycloheximide (CHX, 10 μM), MG-132 (20 μM) and AZD-5438 (5 μM) (CDK2i) (*n* = 1 biological replicates).



Extended Data Fig. 5 | *SF3B1* mutant cells elicit a defective RS response under PARPi.

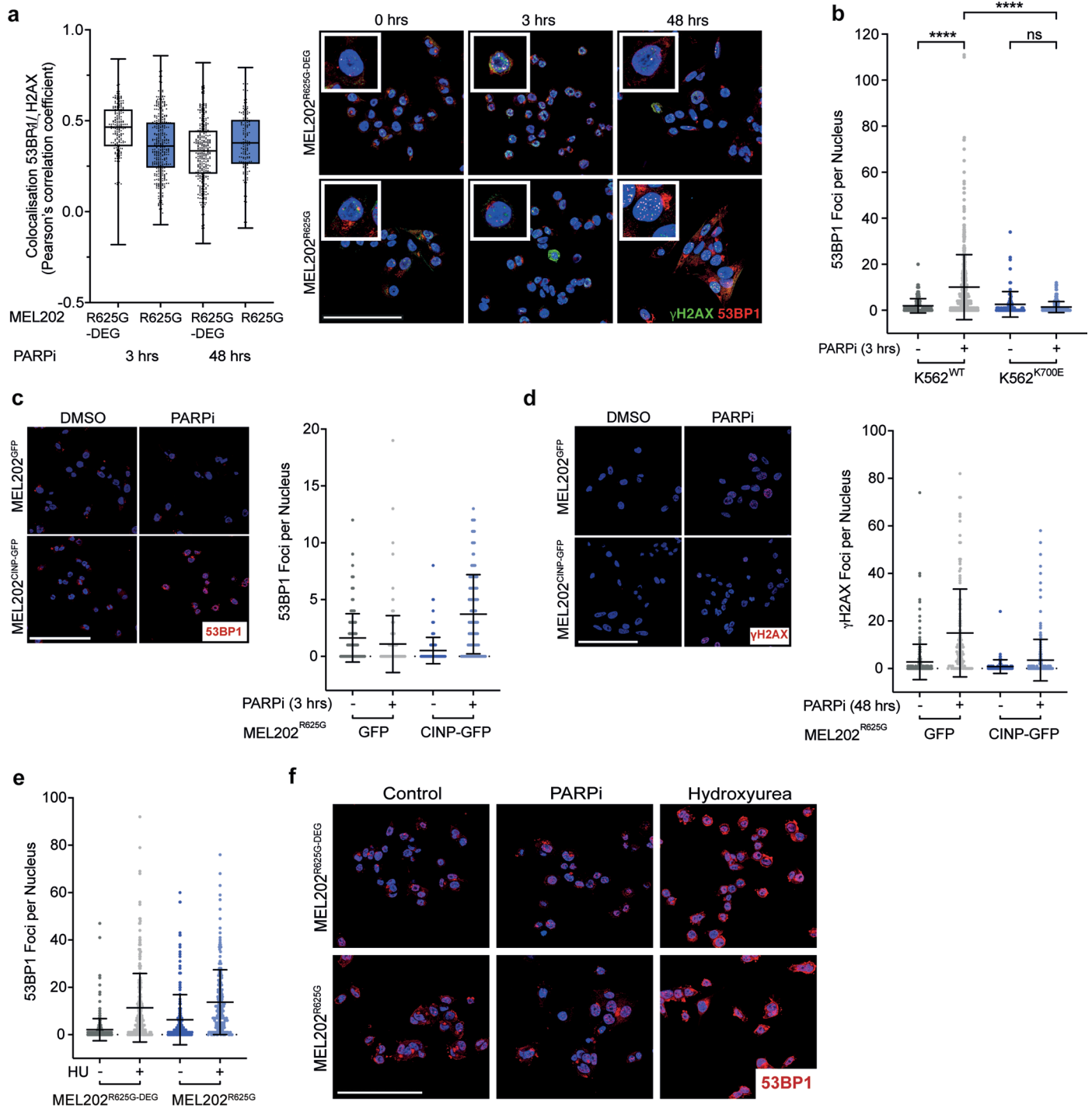
a, Experimental set up of fiber assay and representative immunofluorescence images of IdU and CldU labeled DNA fibers after 3 hours 500 nM talazoparib or DMSO exposure. **b**, Schematic of analysis and scatterplot of quantification of sister fork ratio taken from DNA fiber analysis of MEL202 isogenic cells exposed to DMSO. Data are mean of $n = 3$ biological replicates, error bars show \pm s.e.m. (unpaired two-tailed t-test (NS $P = 0.1337$)). **c**, Representative immunofluorescence images (ci) and scatterplot (cii) of RPA foci in MEL202 isogenic cells following 3 hours of 500 nM talazoparib or DMSO exposure. Data are from $n = 2$ biological replicates, error bars show \pm s.d. of foci in

individual nuclei. Scale bar = 100 μ m. **d**, Western blot of pATR (T1989) in MP41^{WT} and MEL202 isogenic cells (di) and K562 isogenic cells (dii) at 0, 1, or 3 hours of 500 nM talazoparib exposure. **e**, Western blot of pCHK1 (S317), total CHK1, and CINP expression using two different CINP antibodies in MEL202^{R625G-DEG} cells after non-targeting control (NTC) or *CINP* siRNA gene mediated silencing, at 0, 1, or 3 hours of 500 nM talazoparib exposure ($n = 1$ biological replicate). **f**, Scatterplot of CldU/IdU ratio taken from DNA fiber analysis of MEL202 isogenic cells exposed to 100 μ M hydroxyurea (HU). Data are mean of $n = 3$ biological replicates, error bars show \pm s.e.m. (unpaired two-tailed t-test (NS $P = 0.458$)).



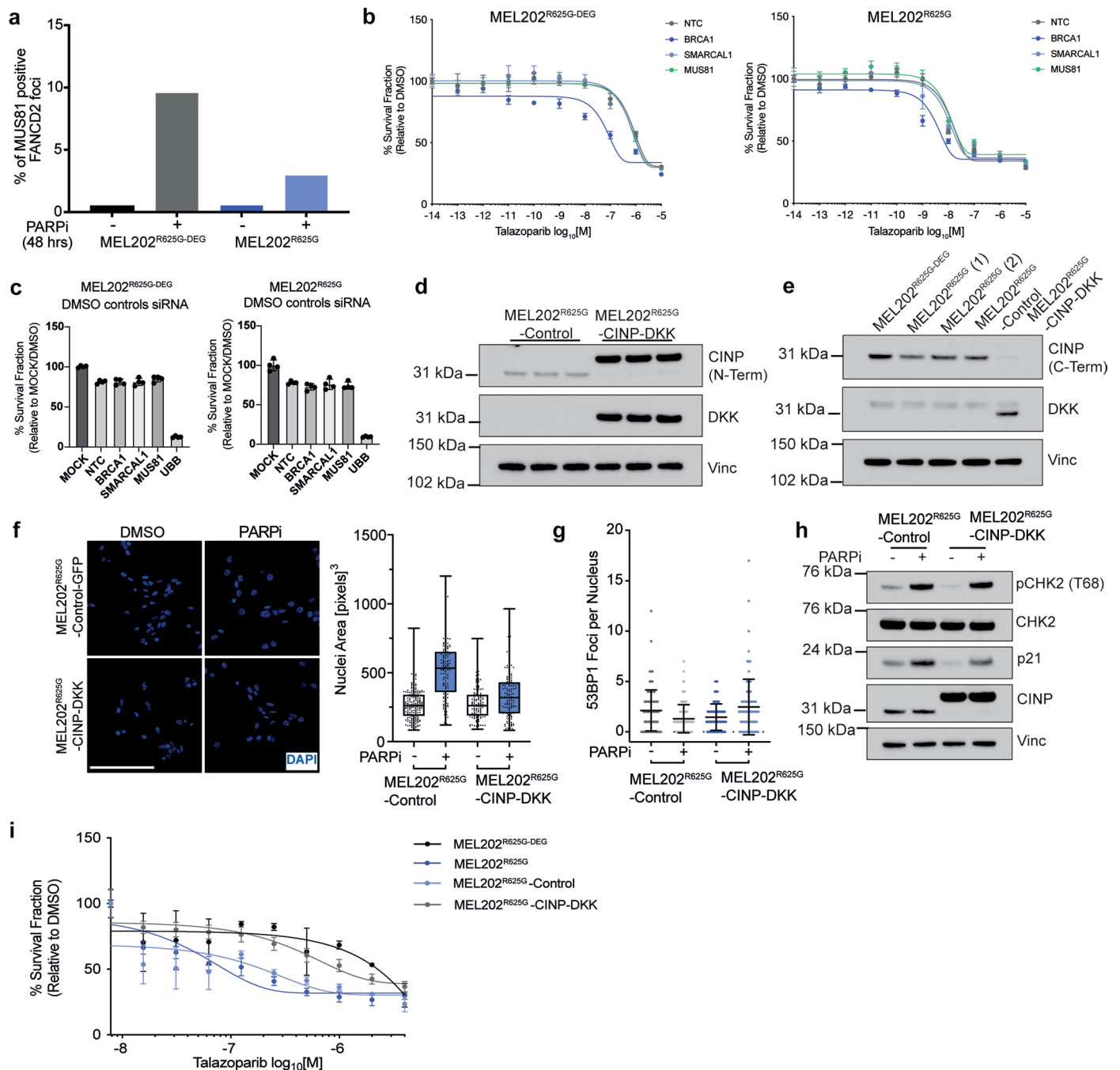
Extended Data Fig. 6 | *SF3B1* mutant cells elicit a replication stress response upon hydroxyurea exposure. a, b, Western blots of pCHK1 (S317) expression in MEL202 isogenic (a) and K562 isogenic cells (b) after 0, 1, and 3 hours of 500 nM talazoparib or 100 μ M hydroxyurea (HU) exposure, and column bar graph showing relative pCHK1 (S317) expression relative to β -Actin loading control.

Images are representative of $n = 2$ biological replicates. **c,** Talazoparib, HU, and gemcitabine dose-response curves showing the survival fraction, relative to DMSO, of MEL202 isogenic cells. Data are mean of at least $n = 2$ biological replicates, error bars show \pm s.d.



Extended Data Fig. 7 | *SF3B1* mutant cells have a defective replication stress regulatory response upon PARPi exposure. **a**, Box and whiskers plot and representative images showing the colocalization of 53BP1 and γH2AX in MEL202 isogenic cells after 3 hours of 500 nM, or 48 hours of 50 nM, talazoparib exposure. Colocalization based on the Pearson's correlation coefficient of the 53BP1 and γH2AX fluorescence intensity per nuclei ($n > 220$ cells from $n = 1$ biological replicate) Scale bar = 100 μm, error bars show \pm s.d. **b**, Scatterplot showing the number of 53BP1 foci per nucleus in K562 isogenic cells after 3 hours of 500 nM talazoparib or DMSO exposure. Data are mean of $n = 3$ biological replicates, error bars show \pm s.d. (unpaired two-tailed t-test (**** $P < 0.0001$,

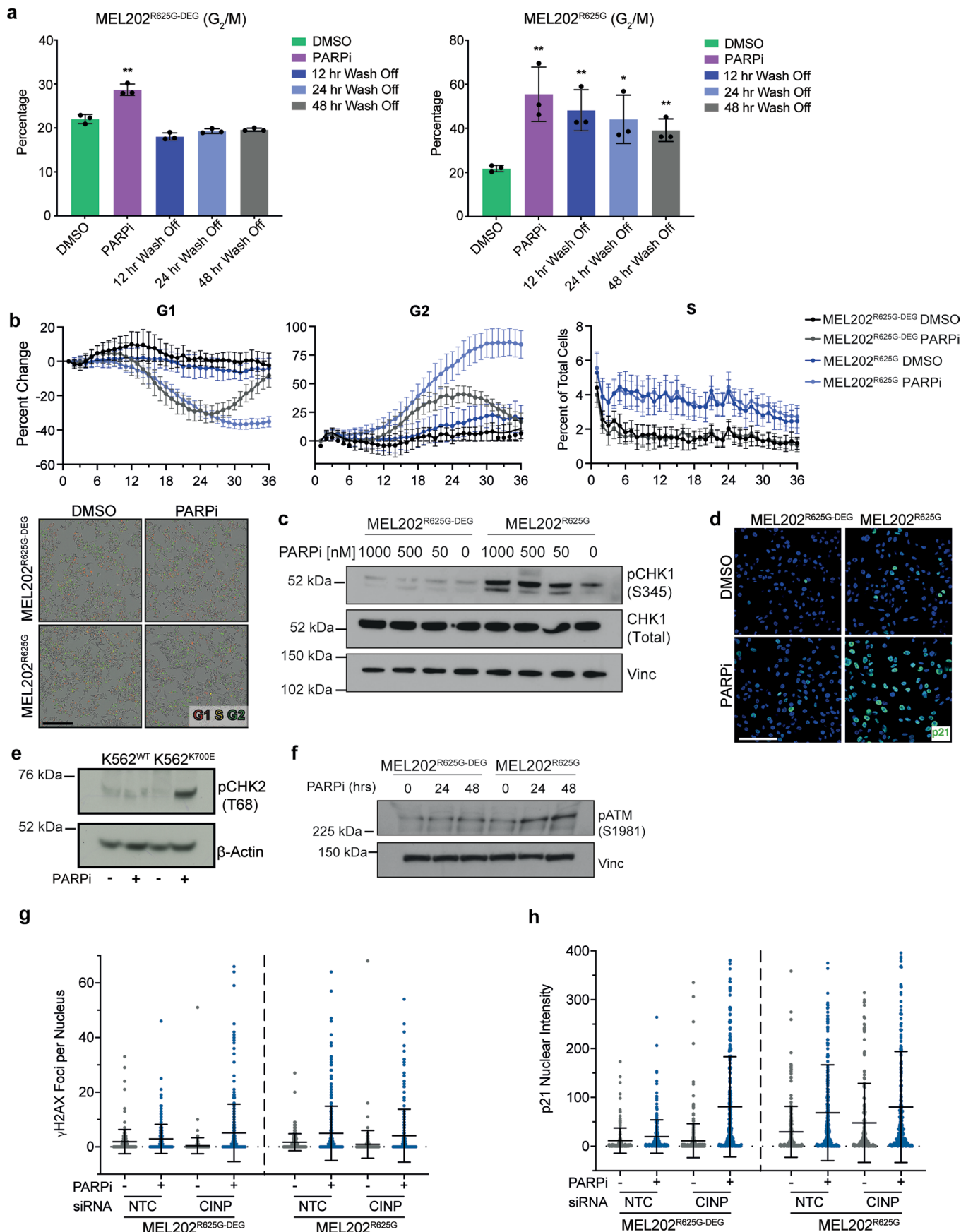
$NS P = 0.238$)). **c-d**, Representative immunofluorescence images and scatter plot quantification of 53BP1 (c) and γH2AX (d) foci in MEL202^{R625G} cells expressing control-GFP or CINP-GFP, treated with 3 hours of 500 nM (c) ($n > 205$ cells from $n = 2$ independent biological replicates) or 48 hours of 50 nM talazoparib (d) ($n > 126$ cells from $n = 1$ biological replicate). Error bars show \pm s.d. **e-f**, Scatter plot quantification and representative immunofluorescence images of 53BP1 foci in MEL202 isogenic cells after 100 μM HU ($n > 214$ cells from $n = 1$ biological replicate), or DMSO exposure. Error bars show \pm s.e.m, 500 nM talazoparib ($n > 215$ cells from $n = 3$ independent biological replicates).



Extended Data Fig. 8 | *SF3B1* mutant cells fail to resolve replication

intermediates under PARPi exposure. **a**, Bar plot showing percentage of MUS81 positive FANCD2 foci in MEL202 isogenic cells after 48 hours of 50 nM talazoparib exposure ($n = 3$ independent biological replicates). **b**, Dose-response of talazoparib exposure after NTC, *BRCA1*, *SMARCAL1* and *MUS81* mediated gene silencing in MEL202^{R625G} cells normalized to DMSO control ($n = 1$ biological replicate, error bars are \pm s.d. of $n = 4$ technical replicates). **c**, Barplot showing cell survival relative to mock transfection of NTC, *BRCA1*, *SMARCAL1* and *MUS81* mediated gene silencing of MEL202^{R625G-DEG} and MEL202^{R625G} DMSO exposed cells from (b) ($n = 1$ biological replicate, error bars are \pm s.d. of $n = 4$ technical replicates). **d**, Western blot showing CINP (N-terminal) and DKK tag expression in MEL202^{R625G} cells expressing control-GFP or CINP-DKK ($n = 1$ biological replicate). **e**, Western blot showing CINP (C-terminal) and DKK tag expression in MEL202 isogenic cells, and MEL202^{R625G} cells expressing control-GFP or

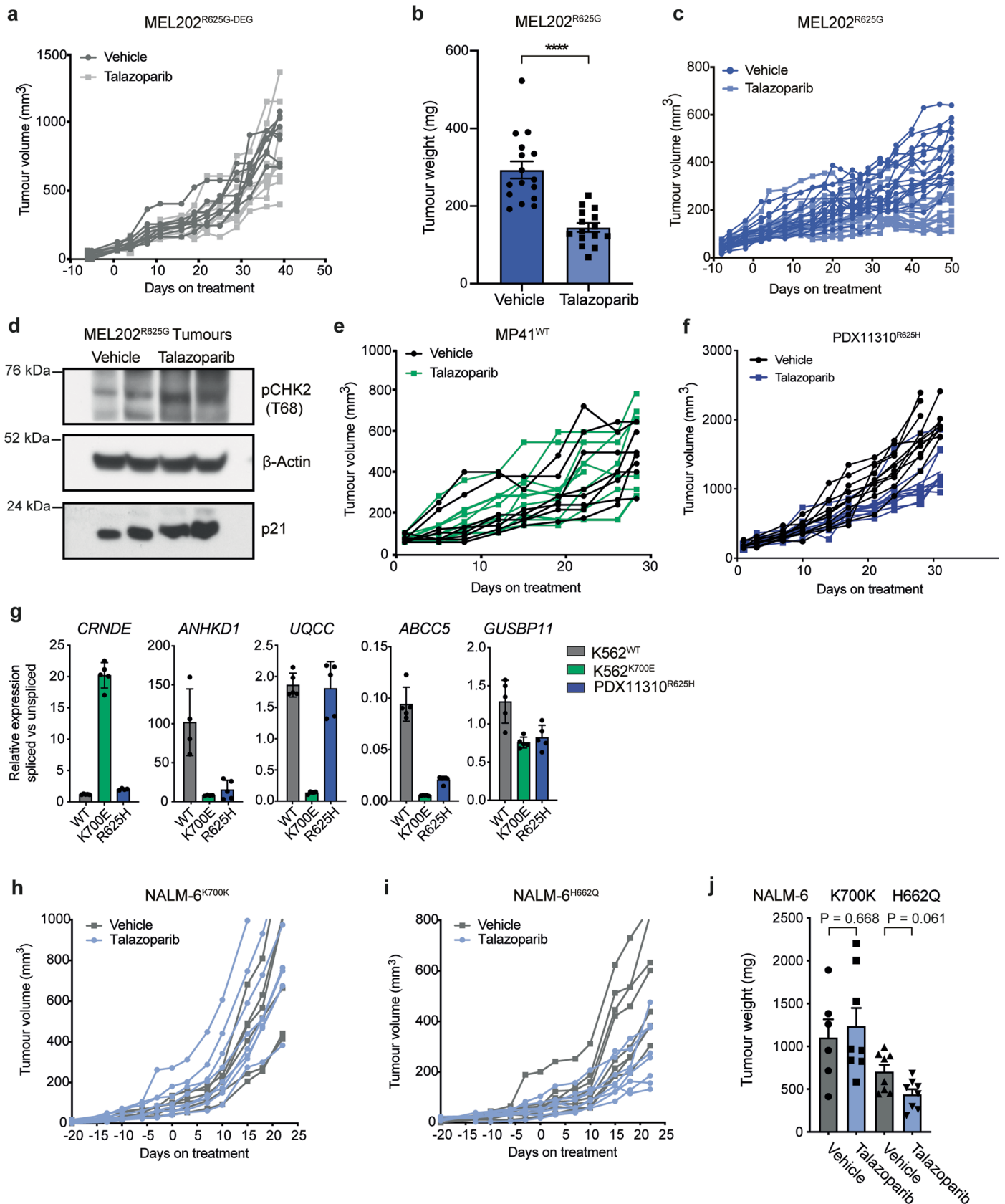
CINP-DKK. **f**, Representative immunofluorescence images and corresponding box and whiskers plot showing the nuclear area of MEL202^{R625G} cells expressing control-GFP or CINP-DKK after 48 hours of 50 nM talazoparib exposure ($n = 1$ biological replicate, error bars show minimum to maximum nuclear area of $n > 125$ individual nuclei assessed). Scale bar = 100 μ m. **g**, Scatterplot showing the number of 53BP1 foci per nucleus in MEL202^{R625G} cells expressing control-GFP or CINP-DKK after 3 hours of 500 nM talazoparib or DMSO exposure ($n = 1$ biological replicate, error bars show \pm s.d. of $n > 81$ individual nuclei assessed). **h**, Western blot showing pCHK2 (T68), total CHK2, p21, and CINP (N-terminal) expression in MEL202^{R625G} cells expressing control-GFP or CINP-GFP, treated with 48 hours of 50 nM talazoparib ($n = 1$ biological replicate). **i**, Talazoparib 5-day dose-response curves of MEL202 isogenic cells, and MEL202^{R625G} cells expressing control-GFP or CINP-DKK ($n = 1$ biological replicate). Data are presented as mean values \pm s.d. of $n = 4$ technical replicates.



Extended Data Fig. 9 | See next page for caption.

Extended Data Fig. 9 | The induction of the G₂/M checkpoint in *SF3B1* mutant cells. **a**, Column bar graphs showing the increase in percentage of MEL202^{R625G-DEG} and MEL202^{R625G} isogenic cells in G₂/M phase after 48 hours of 50 nM talazoparib exposure, and 12, 24, and 48 hours after talazoparib removal. Data are mean of $n = 3$ biological replicates, error bars show \pm s.e.m. (unpaired two-tailed t-test (MEL202^{R625G-DEG} $**P = 0.0022$ and MEL202^{R625G} $**P = 0.0094$, $**P = 0.0084$, $*P = 0.0249$, $**P = 0.0049$)). **b**, Time-course assessment of the proportion of MEL202^{R625G-DEG} and MEL202^{R625G} cells in each of G1 (red) and G2 (green) phase of the cell cycle over 36 hours treated with DMSO or 50 nM talazoparib plotted relative to time 0. S phase is determined by spectral overlap (red and green) and is plotted as percent of total number of cells. Representative micrographs at 36 hours are shown. Data is representative of $n = 2$ biological replicates (Scale bar = 400 μ m). **c**, Western blot of pCHK1 (S345) and total CHK1 expression in

MEL202^{R625G-DEG} and MEL202 isogenic cells after 48 hours of 1000 nM, 500 nM, 50 nM, or 0 nM talazoparib exposure. **d**, Representative immunofluorescence images to corresponding Fig. 5c showing the nuclear intensity of p21 in MEL202^{R625G} cells, after 48 hours of 50 nM talazoparib or DMSO exposure. **e**, Western blot of pCHK2 (T68) expression in K562 isogenic cells after 48 hours of 50 nM talazoparib or DMSO exposure. Data are representative of $n = 2$ biological replicates. **f**, Western blot of pATM (S1981) expression in MEL202 isogenic cells after 24 or 48 hours of 50 nM talazoparib or DMSO exposure. Images are representative of two biological replicates. **g-h**, Scatter plot quantification of γ H2AX (g) and p21 (h) in MEL202 isogenic cells after NTC or *CINP* gene silencing after 48 hours 50 nM talazoparib exposure. Data are of $n = 1$ biological replicate, error bars show \pm s.d.



Extended Data Fig. 10 | See next page for caption.

Extended Data Fig. 10 | PARPi suppresses *SF3B1* mutant tumor growth

in vivo. **a**, Chart depicting individual tumor volumes of the therapeutic response to talazoparib treatment in NSG-Nude mice bearing MEL202^{R625G-DEG} xenograft tumors over time, (0.33 mg/kg). Day 0 represents the first day of treatment, (Fig. 5a). **b**, Bar plot of tumor weights from MEL202^{R625G} subcutaneous tumors under treatment. At the experimental end-point, tumors were resected and weighed *ex vivo* (unpaired two-tailed t-test, **** $P < 0.0001$). **c**, Chart depicting individual tumor volumes of the therapeutic response to talazoparib treatment in NSG-Nude mice bearing *SF3B1* mutant MEL202^{R625G} xenograft tumors over time, (0.33 mg/kg). Day 0 represents the first day of treatment, (Fig. 5b). **d**, Western blot of CHK2 phosphorylation at threonine 68 (pCHK2 (T68)) in two MEL202^{R625G} xenograft tumors at end-point treatment with either vehicle control

or talazoparib. **e, f**, Charts depicting individual tumor volumes of the therapeutic response to talazoparib treatment in NOD-SCID mice bearing *SF3B1*^{WT} PDX MP41 (e) and *SF3B1*^{R625H} PDX11310 patient derived xenograft (f) tumors over time, (0.33 mg/kg). Day 0 represents the first day of treatment. **g**, qRT-PCR of differentially spliced exons of indicator genes in the PDX11310 *in vivo* model. Data are mean of $n = 3$ biological replicates, error bars show \pm s.e.m. **h, i**, Charts depicting individual tumor volumes of the therapeutic response to talazoparib treatment in CB-17 mice bearing the *SF3B1*^{MULT} NALM6^{H662Q} (i) and NALM6^{K700K} (h) leukemia xenograft tumors over time, (0.33 mg/kg). Day 0 represents the first day of treatment. **j**, Bar plot of tumor weights from NALM-6 subcutaneous tumors under treatment, at the experimental end-point, tumors weighed *ex vivo*. P values shown are calculated using an unpaired two-tailed t-test.

Reporting Summary

Nature Portfolio wishes to improve the reproducibility of the work that we publish. This form provides structure for consistency and transparency in reporting. For further information on Nature Portfolio policies, see our [Editorial Policies](#) and the [Editorial Policy Checklist](#).

Statistics

For all statistical analyses, confirm that the following items are present in the figure legend, table legend, main text, or Methods section.

n/a Confirmed

- The exact sample size (n) for each experimental group/condition, given as a discrete number and unit of measurement
- A statement on whether measurements were taken from distinct samples or whether the same sample was measured repeatedly
- The statistical test(s) used AND whether they are one- or two-sided
Only common tests should be described solely by name; describe more complex techniques in the Methods section.
- A description of all covariates tested
- A description of any assumptions or corrections, such as tests of normality and adjustment for multiple comparisons
- A full description of the statistical parameters including central tendency (e.g. means) or other basic estimates (e.g. regression coefficient) AND variation (e.g. standard deviation) or associated estimates of uncertainty (e.g. confidence intervals)
- For null hypothesis testing, the test statistic (e.g. F , t , r) with confidence intervals, effect sizes, degrees of freedom and P value noted
Give P values as exact values whenever suitable.
- For Bayesian analysis, information on the choice of priors and Markov chain Monte Carlo settings
- For hierarchical and complex designs, identification of the appropriate level for tests and full reporting of outcomes
- Estimates of effect sizes (e.g. Cohen's d , Pearson's r), indicating how they were calculated

Our web collection on [statistics for biologists](#) contains articles on many of the points above.

Software and code

Policy information about [availability of computer code](#)

Data collection

All histological slides were scanned at x 40 (0.25 $\mu\text{m}/\text{pixel}$) digital magnification using Hamamatsu Nanozoomer XR (Hamamatsu photonics, Hamamatsu, Japan). Digital images in .ndpi format were submitted for quantitative image analysis using HistoQuest 6.0 (Tissugnostic, Vienna, Austria) software or QPath v0.3.0.
Clonogenic survival assays were quantified using MATLAB.
Immunofluorescence slides were imaged on a Leica SP8 Confocal Microscope. Mitotic phase analysis of the MEL202R625G-DEG and MEL202R625G cell lines was imaged using the Zeiss Axio Observer Z1 Advanced Marianas™ Microscope attached with a CSU-W1 SoRa and quantified by eye.

Data analysis

Statistical analysis was carried out using R 3.5.0 (www.r-project.org) and GraphPad Prism 9.
RNA sequencing FASTQ files were aligned to the human genome (hg38) using STAR v2.5.1b with the additional custom parameters '--twopassMode Basic --outSAMstrandField intronMotif --outSAMattributes NH HI AS nM NM XS' with transcript annotations obtained from GENCODE version 22.
Differential gene expression analysis was performed using a negative binomial generalised log-linear model (glmQLFit and glmQLFTest) implemented in edgeR v3.34.0. Normalisation factors to correct for variable sequencing depth and composition bias were calculated using the using the Trimmed Mean of M-values (TMM) method (calcNormFactors). Gene Set Enrichment Analysis was performed with FGSEA version 1.4.1 using the c2.cp.reactome gene sets obtained from the Broad Institute with the minimum pathway size set to 10.
Quantification of PSI values for the alternative splicing event types (Alternative '5, Alternative '3, Exon skip, Multiple Exon Skip, Intron Retention) was performed with spladder (development version dated: 20180703) under default settings (confidence level = 3). rMATS v4.1.2 under default parameters was used as second method to identify and quantify alternative splicing events. Detection of differential alternative splicing events from both spladder and rMATS between K562 SF3B1WT and SF3B1K700E cells was assessed by performing a differential PSI

analysis using the limma v3.48.3. Sequence motif logos illustrating 30 bp upstream and 3bp downstream of significant alternative 3' acceptor splice sites were generated using ggseqlogo v0.1.

RNA PolII ChIP-seq data were mapped to the genome using BWA algorithm vv0.7.12 with default settings and hg38 reference genome. Only reads that passed Illumina's purity filter, aligned with no more than 2 mismatches, and mapped uniquely to the genome were used in the subsequent analysis. Peaks were called using the SICER v1.1.

Clonogenic assay NALM-6 and K562 cell lines were imaged without fixation and quantified on MATLAB vR20018b(9.5.0)

For the proteomics data, the raw files were processed with Proteome Discoverer 2.3 (Thermo Fisher) and searched using both SequestHT and Mascot (v2.3 MatrixScience) against UniProt Human Reference Proteome database (January 2018) concatenated with the cRAP contaminate sequences.

Immunofluorescence was quantified using CellProfiler (version 3.1.9). Foci were counted using the "Speckle Counting" pipeline, while phosphor-histone H3, Cajal Body, p21 and nuclear area analysis was performed using the "Cell/particle counting and scoring the percentage of stained objects" pipeline.

For manuscripts utilizing custom algorithms or software that are central to the research but not yet described in published literature, software must be made available to editors and reviewers. We strongly encourage code deposition in a community repository (e.g. GitHub). See the Nature Portfolio [guidelines for submitting code & software](#) for further information.

Data

Policy information about [availability of data](#)

All manuscripts must include a [data availability statement](#). This statement should provide the following information, where applicable:

- Accession codes, unique identifiers, or web links for publicly available datasets
- A description of any restrictions on data availability
- For clinical datasets or third party data, please ensure that the statement adheres to our [policy](#)

The data that support the findings of this study are available in the Supporting Information. The RNA sequencing data have been deposited in NCBI Sequence Read Archive (SRA) under accession number PRJNA849566; ChIP-seq data PRJNA968072 and the mass spectrometry proteomics data have been deposited to the ProteomeXchange Consortium via the PRIDE partner repository with the dataset identifier PXD019046.

SF3B1 mutations were collated from cBioPortal <https://www.cbioportal.org/querying> MSK-IMPACT PanCancer Clinical Sequencing cohort and TCGA Pan Cancer Atlas studies. Database access 07/2020. UniProt Human Reference Proteome database (January 2018) was used as a reference for the Mass-Spectrometry data.

Human research participants

Policy information about [studies involving human research participants and Sex and Gender in Research](#).

Reporting on sex and gender

Population characteristics

Recruitment

Ethics oversight

Note that full information on the approval of the study protocol must also be provided in the manuscript.

Field-specific reporting

Please select the one below that is the best fit for your research. If you are not sure, read the appropriate sections before making your selection.

Life sciences Behavioural & social sciences Ecological, evolutionary & environmental sciences

For a reference copy of the document with all sections, see [nature.com/documents/nr-reporting-summary-flat.pdf](https://www.nature.com/documents/nr-reporting-summary-flat.pdf)

Life sciences study design

All studies must disclose on these points even when the disclosure is negative.

Sample size

Data exclusions	No mice were excluded
Replication	Sample sizes were sufficiently powered to enable robust reproducibility. Aside from in vivo experiments, replicate experiments were performed in single, duplicate or triplicate independent biological replicates as stated in the figure legends. All data was reproduced in replicate experiments.
Randomization	Animals were randomised when tumours reached 100mm ³ . All other experiments were allocated into experimental groups based on treatment (PARPi or control) and/or SF3B1 mutation status (mutant or wild-type).
Blinding	For all in vivo studies, the investigators were blinded to group allocations and dosing was performed by independent lab technicians.

Reporting for specific materials, systems and methods

We require information from authors about some types of materials, experimental systems and methods used in many studies. Here, indicate whether each material, system or method listed is relevant to your study. If you are not sure if a list item applies to your research, read the appropriate section before selecting a response.

Materials & experimental systems

n/a	Included in the study
<input type="checkbox"/>	<input checked="" type="checkbox"/> Antibodies
<input type="checkbox"/>	<input checked="" type="checkbox"/> Eukaryotic cell lines
<input checked="" type="checkbox"/>	<input type="checkbox"/> Palaeontology and archaeology
<input type="checkbox"/>	<input checked="" type="checkbox"/> Animals and other organisms
<input type="checkbox"/>	<input checked="" type="checkbox"/> Clinical data
<input checked="" type="checkbox"/>	<input type="checkbox"/> Dual use research of concern

Methods

n/a	Included in the study
<input type="checkbox"/>	<input checked="" type="checkbox"/> ChIP-seq
<input type="checkbox"/>	<input checked="" type="checkbox"/> Flow cytometry
<input checked="" type="checkbox"/>	<input type="checkbox"/> MRI-based neuroimaging

Antibodies

Antibodies used

Table S9. Antibodies and dilutions

Catalogue No.	Supplier	Antibody	Dilution	Application	in this study	Lot Number
MAB3802	Millipore	Anti-53BP1 Antibody, clone BP13	1:1000	IF		3524755
ab180955	Abcam	Anti-CINP antibody [EPR14446]	ab180955 1:1000	WB, IHC		GR148706-2
AB87913	Abcam	Anti-Coilin antibody [IH10] (ab87913)	100ug 1:1000	IF		GR3218582-3
7076S	Cell Signalling Technology	Anti-mouse IgG, HRP-linked Antibody #7076	1:5000	WB		36
05-636	Millipore	Anti-phospho-Histone H2A.X (Ser139) Antibody, clone JBW301	1:1000	IF		3313712
7074S	Cell Signalling Technology	Anti-rabbit IgG, HRP-linked Antibody #7074	1:5000	WB		30
NA18	Millipore	Anti-Replication Protein A (Ab-2) Mouse mAb (RPA34-19)	1:200	IF		3173547
30632S	Cell Signalling Technology	ATR (phospho Thr1989) antibody	1:1000	WB		1
2360S	Cell Signalling Technology	Chk1 (2G1D5) Mouse mAb #2360	1:1000	WB		3
2639S	Cell Signalling Technology	Fibrillarin (C13C3) Rabbit mAb #2639	1:1000	IF		2
ab133741	Abcam	Lamin B1 1:1000	WB			GR3244890-2
3873S	Cell Signalling Technology	Monoclonal Anti- α -Tubulin antibody produced in mouse	1:1000	WB		16
2947T	Cell Signalling Technology	p21 Waf1/Cip1 (12D1) Rabbit mAb #2947	1:1000	WB, IF		11
2344S	Cell Signalling Technology	Phospho-Chk1 (Ser317) Antibody #2344	1:1000	WB		12
2348S	Cell Signalling Technology	Phospho-Chk1 (Ser345) (133D3) Rabbit mAb #2348	1:1000	WB		18
2197S	Cell Signalling Technology	Phospho-Chk2 (Thr68) (C13C1) Rabbit mAb	1:1000	WB		12
53348S	Cell Signalling Technology	Phospho-Histone H3 (Ser10) (D7N8E) XP [®] Rabbit mAb #53348	1:1000	IF		1
ab183519	Abcam	Recombinant Anti-CINP antibody [EPR14445] - N-terminal	1:1000	WB		GR153682-4
ab133534	Abcam	Recombinant Anti-Rad51 antibody [EPR4030(3)]	1:1000	IF		GR219215-42
2808S	Cell Signalling Technology	Survivin (71G4B7) Rabbit mAb #2808	1:1000	WB, IF		15
18799S	Cell Signalling Technology	Vinculin (E1E9V) XP [®] Rabbit mAb (HRP Conjugate)	1:1000	WB		2
sc53382	Santa Cruz	MUS81 (MTA30 2G10/3) mouse mAb monoclonal	1/100	1:1000	IF	G0721
NB100-182	Novus	FANCD2 Rabbit polyclonal Ab	1/400	1:400	IF	S-5
4526S	Cell Signalling Technology	Phospho-ATM (Ser1981) (10H11.E12) Mouse mAb	1:1000	WB		14
2978S	Cell Signalling Technology	Cyclin D1 (92G2) Rabbit mAb	1:1000	WB		13
2737S	Cell Signalling Technology	ATRIP Antibody (Rabbit)	1:1000	WB		2
14793S	Cell Signalling Technology	DYKDDDDK Tag (D6W5B) Rabbit mAb	1:1000	WB		7
5125S	Cell Signalling Technology	β -Actin (13E5) Rabbit mAb (HRP Conjugate)	1:5000	WB		6
ab26721	Abcam	Anti-RNA polymerase II CTD repeat YSPTSPS antibody - ChIP Grade	1:1000	WB	n/a	
MABE954	Sigma-Aldrich	Anti-phospho RNA Pol II (Ser5), clone 1H4B6	Antibody 1:1000	WB		3512558
MABE953	Sigma-Aldrich	Anti-phospho RNA Pol II (Ser2), clone 3E7C7	Antibody 1:1000	WB		3692727
A300-996A	Bethyl Laboratories	SF3b155/SAP155 Polyclonal Antibody	1:1000	WB		1
WH0000142M1	Sigma-Aldrich	Anti-PARP1 Monoclonal Antibody	1:1000	WB		KC101-3G4
ab51052	Abcam	Recombinant Anti-Hsc70 Rabbit mAb (EP1531Y)	1:1000	WB	n/a	
39097	Active Motif	Anti- RNA Polymerase II (total) Mouse mAb (Clone H48)	20uL 4ug	(ChIP-seq)		WB 19
347580	BD Biosciences	anti- BrdU. Mouse mAb Clone 3D4 (RUO)	1:20	IF		2077345
ab6326	Abcam	anti- BrdU. rat mAb	1:400	IF		GR3365969-8

Validation

Table S9. Antibodies and dilutions

Catalogue No. Validated in this study Validation by company
 MAB3802 WB, ChIP, Flow, Flow-IC, IB, ICC/IF, IHC, IHC-Fr, IHC-P, IP, ISH, KD, KO
 ab180955 KD WB, IP
 AB87913 WB, ICC, IP, IHC-P, Flow, KO
 7076S WB
 05-636 WB, IF, ICC, ChIP
 7074S WB
 NA18 IF, IP
 30632S WB
 2360S WB, KD
 2639S WB, IF
 ab133741 WB, IP, ICC/IF, IHC-P, IP, KO
 3873S WB, IHC-P, ICC/IF, Flow
 2947T WB, IP, IHC, IF, Flow, KO
 2344S WB
 2348S WB, IF, Flow
 2197S WB, IP, IHC, Flow
 53348S WB, IP, ICC/IF, ChIP, Flow
 ab183519 KD WB, ICC/IF, IP
 ab133534 WB, IHC-P, ICC/IF, IP, Flow
 2808S WB, IP, IHC-P, ICC/IF, Flow, KD
 18799S WB
 sc53382 WB, IP
 NB100-182 WB, ChIP, Flow, IB, ICC/IF, IHC, IHC-P, IP, KD, KO
 4526S WB
 2978S WB, IHC-P
 2737S WB, IF, IP
 14793S WB, IP, IHC-P, ICC/IF, Flow, ChIP
 5125S WB
 ab26721 WB, IHC-P, IP, ICC/IF, ChIP
 MABE954 WB, ChIP-Seq, ICC, ELISA & ChIP
 MABE953 WB, ICC, ELISA, ChIP
 A300-996A WB, IP
 WH0000142M1 KO WB, ELISA, IF
 ab51052 IP, Flow-IC, WB, IHC-P, ICC/IF, KO
 39097 WB, ChIP, ChIP-Seq
 347580 Flow-IC
 ab6326 ICC/IF, IHC-P, Flow-IC

Key

WB Western Blot
 ChIP Chromatin Immunoprecipitation
 Flow Flow cytometry
 Flow-IC Flow intracellular
 IB Immunoblotting
 ICC/IF Immunocytochemistry/Immunoblotting
 IHC Immunohistochemistry
 IHC-Fr Immunohistochemistry-Frozen
 IHC-P Immunohistochemistry-Paraffin
 IP Immunoprecipitation
 ISH In situ hybridisation
 KD Knock down validated
 KO Knock out validated

Eukaryotic cell lines

Policy information about [cell lines and Sex and Gender in Research](#)

Cell line source(s)

All cell lines used in the study are derived from human.
 RRID:CVCL_0004. K562 - Female parental SF3B1WT, control edited synonymous mutated SF3B1K700K and mutant SF3B1K700E and SF3B1K666N; and RRID:CVCL_0092. NALM-6 - Male-parental SF3B1WT, control edited synonymous mutated SF3B1K700K and mutated SF3B1H662Q, SF3B1K700E, SF3B1K666N engineered isogenic cell lines were obtained from Horizon Discovery.
 RRID:CVCL_C301. MEL202 Female parental cell line was provided by the originator Bruce Kasander Schepens Eye Research Institute; Boston; USA
 RRID:CVCL_4D13. MP46 Female patient derived xenograft cell line was provided by the originators Fariba Nemati and Marc Henri-Stern (Institute Curie, France)
 RRID:CVCL_C302. MEL270 Male cell line was provided by the originator Bruce Kasander Schepens Eye Research Institute; Boston; USA

	RRID:CVCL_4D12. MP41 Female patient derived xenograft cell line was provided by the originators Fariba Nemati and Marc Henri-Stern (Institute Curie, France)
Authentication	All cell lines were authenticated using STR profiling with the Geneprint10 Kit (Promega) and were sequenced to check the retention of engineered alterations during culture
Mycoplasma contamination	All cell lines were tested monthly to confirm no mycoplasma infection using the Mycoalert™ Mycoplasma Detection Kit as per manufacturer's instructions. All cell lines used in the study tested negative for mycoplasma infection.
Commonly misidentified lines (See ICLAC register)	No mis-identified lines were used in this study

Animals and other research organisms

Policy information about [studies involving animals](#); [ARRIVE guidelines](#) recommended for reporting animal research, and [Sex and Gender in Research](#)

Laboratory animals	7-8 week old female CB-17 (NOD.CB17-Prkdcscid/J), NSG-Nude (NOD.Cg-Foxn1em1Dvs Prkdcscid Il2rgtm1Wjl/J) and NOD-SCID (NOD.Cg-Prkdcscid/J) immuno-compromised mice were purchased from the Jackson Laboratory. All animals were maintained at 24-26°C ambient temperature with 55% humidity. Mice were subject to 12 hour dark-light cycles.
Wild animals	This study did not involve wild animals.
Reporting on sex	Female mice were used in this study
Field-collected samples	This study did not involve samples collected from the field.
Ethics oversight	The in vivo studies carried out at The Institute of Cancer Research were performed to ARRIVE guidelines and regulations as described in the UK Animals Scientific Procedures Act 1986 and according to the UK Home Office projected licences held by CJL and approved by the ethics board at The Institute of Cancer Research (maximum tumour size 15mm diameter). Additional in vivo studies were performed to local regulatory guidelines at Institut Curie (MP41 and MEL202R625G-DEG) (CEEA-IC #118, Authorization APAFIS #25870-2020060410487032-v1 given by National Authority, maximal tumour volume 2500mm ³) and Crown Biosciences USA (PDX11310) (maximum tumour size 2000mm ³). The maximal tumour size was not exceeded. Patients that provided samples from which PDX were generated were appropriately and fully consented.

Note that full information on the approval of the study protocol must also be provided in the manuscript.

Clinical data

Policy information about [clinical studies](#)

All manuscripts should comply with the ICMJE [guidelines for publication of clinical research](#) and a completed [CONSORT checklist](#) must be included with all submissions.

Clinical trial registration	The trial is registered with ISRCTN registry (ISRCTN34386131)
Study protocol	This is available in the original publication Pratt et al doi:10.1111/bjh.14793
Data collection	This is available in the original publication Pratt et al doi:10.1111/bjh.14793
Outcomes	This is available in the original publication Pratt et al doi:10.1111/bjh.14793

ChIP-seq

Data deposition

- Confirm that both raw and final processed data have been deposited in a public database such as [GEO](#).
- Confirm that you have deposited or provided access to graph files (e.g. BED files) for the called peaks.

Data access links <i>May remain private before publication.</i>	<i>For "Initial submission" or "Revised version" documents, provide reviewer access links. For your "Final submission" document, provide a link to the deposited data.</i>
Files in database submission	SRR24460485 PRJNA968071 SAMN34896536 Pooled_Input Pooled_Input SRR24460487 PRJNA968071 SAMN34896534 K700K-WT_Pol2 K700K-WT_Pol2 SRR24460486 PRJNA968071 SAMN34896535 K700E-MUT_Pol2 K700E-MUT_Pol2 SRR24460488 PRJNA968071 SAMN34896533 Parental_Pol2 Parental_Pol2
Genome browser session (e.g. UCSC)	No longer applicable

Methodology

Replicates	Experiments were performed as a single replicate
Sequencing depth	Single end sequencing 75bp read length. Total number of reads: K562WT- 35,559,728; K562K700K-39,011,608; K562K700E-37,079,970 Total mapped(aligned reads): K562WT- 32,001,086; K562K700K-34,594,764; K562K700E-34,072,899 Uniquely mapped reads: K562WT- 28,995,696; K562K700K-31,119,159; K562K700E-30,724,511
Antibodies	39097 Active Motif Anti- RNA Polymerase II (total) Mouse mAb 4ug (20uL).
Peak calling parameters	RNA Pol2-enriched regions were identified using the SICER algorithm v. 1.1 at a cutoff of FDR 1E-10 and a max gap parameter of 600 bp.
Data quality	Peaks that were on the ENCODE blacklist of known false ChIP-Seq peaks were removed. Signal maps and peak locations were used as input data to Active Motifs proprietary analysis program, which creates Excel tables containing detailed information on sample comparison, peak metrics, peak locations and gene annotations. Filtered peaks: K562WT- 22,534; K562K700K-20,278; K562K700E-20,262
Software	BWA (v0.7.12) genome alignment SICER (v1.1) (peak calling) bcl2fastq2 (v2.20) (processing of Illumina base-call data and demultiplexing) Samtools (v0.1.19) (processing of BAM files) BEDtools (v2.25.0) (processing of BED files) wigToBigWig (v4) (generation of bigWIG files)

Flow Cytometry

Plots

Confirm that:

- The axis labels state the marker and fluorochrome used (e.g. CD4-FITC).
- The axis scales are clearly visible. Include numbers along axes only for bottom left plot of group (a 'group' is an analysis of identical markers).
- All plots are contour plots with outliers or pseudocolor plots.
- A numerical value for number of cells or percentage (with statistics) is provided.

Methodology

Sample preparation	Cell-cycle analysis was undertaken using propidium iodide (PI) (Abcam, ab14083) and analysed on BD LSRII cell analyser. Trypsinised cells were washed twice in PBS before fixation through the dropwise addition of 70% ethanol and allowed to fix for 30 min at 4°C. Cell pellets were washed twice with PBS at 850 g and then treated with 50 ul of 100 ug/ml RNase. Finally, 200 ul of 50 ug/ml PI was used to resuspend the cell pellet ready for analysis.
Instrument	All samples were processed on the BD LSRII cell analyser
Software	FlowJO (BD biosciences) analysis software.
Cell population abundance	No sorting was performed.
Gating strategy	Forward and side scatters were set to identify single cells and doublets were excluded. Gates were then automatically set and percentages derived by use of FlowJO (BD biosciences) analysis software.

- Tick this box to confirm that a figure exemplifying the gating strategy is provided in the Supplementary Information.